

63p  
CONFIDENTIAL

62 71989 Copy 612

NASA TM X-165

NASA

Classification changed to declassified  
effective 1 April 1968 under  
Authority of NASA OCS 2 by  
Carroll.

N63-13896  
CODE-1

# TECHNICAL MEMORANDUM

X-165

TRANSONIC OFF-DESIGN PERFORMANCE OF A FIXED

DIVERGENT EJECTOR DESIGNED FOR A

MACH NUMBER OF 2.0

By Harry T. Norton, Jr., Marlowe D. Cassetti,  
and Charles E. Mercer

Langley Research Center  
Langley Field, Va.

[REDACTED]

WEP 553988

CLASSIFIED DOCUMENT - TITLE UNCLASSIFIED

This material contains information affecting the national defense of the United States within the meaning of the espionage laws, Title 18, U.S.C., Secs. 793 and 794, the transmission or revelation of which in any manner to an unauthorized person is prohibited by law.

NATIONAL AERONAUTICS AND SPACE ADMINISTRATION

WASHINGTON

December 1959

CONFIDENTIAL

UNCLASSIFIED

NATIONAL AERONAUTICS AND SPACE ADMINISTRATION

TECHNICAL MEMORANDUM X-165

TRANSONIC OFF-DESIGN PERFORMANCE OF A FIXED

DIVERGENT EJECTOR DESIGNED FOR A

MACH NUMBER OF 2.0\*

By Harry T. Norton, Jr., Marlowe D. Cassetti,  
and Charles E. Mercer

SUMMARY

An investigation of a pylon-supported nacelle model with a fixed divergent ejector has been conducted in the Langley 16-foot transonic tunnel over a Mach number range from 0.90 to 1.06. The divergent ejector was designed for a Mach number of 2.0 and a primary jet total-pressure ratio of 10.1 with an afterburning primary nozzle and a corrected secondary weight-flow ratio of 0.042. The jet exhaust was simulated with a hydrogen peroxide turbojet simulator. The average Reynolds number based on nacelle length was  $20 \times 10^6$ .

The results of the investigation indicate that, for values of primary jet total-pressure ratio and corrected weight-flow ratio corresponding to a typical turbojet-engine schedule, satisfactory performance was obtained with the nonafterburning nozzle configuration over the Mach number range from 0.90 to 1.00. However, the nonafterburning configuration experienced a large loss in performance when the primary jet total-pressure ratio was equal to a value for which the jet was just attached to the divergent wall of the ejector. The afterburning nozzle configuration experienced large off-design losses in performance over the Mach number range of the investigation due to overexpansion of the primary jet.

INTRODUCTION

Several investigations have been conducted to determine the efficiency of the divergent shroud-ejector nozzle. (For example, see refs. 1 and 2.) The results of these investigations have shown that the divergent

---

\*Title, Unclassified.

CONFIDENTIAL

CONFIDENTIAL

ejector configuration provides a more efficient thrust system at the higher primary jet pressure ratios than a convergent nozzle and also indicate that the divergent nozzle should be variable in order to operate efficiently over the pressure ratio range. The variable divergent nozzle would also require that the external arrangement of the afterbody vary in order to adjust to the change in the divergent nozzle exit area and to maintain a shape having low external drag.

Because of the weight and complexity of a combination of a variable divergent shroud ejector and nozzle, consideration has been given to combinations of a fixed divergent shroud ejector and afterbody designed for a Mach number of 2.0 which will operate over the speed range without excessive thrust and drag penalties. An investigation of the off-design performance of such a fixed divergent ejector is reported in reference 3. Further work on a similar fixed divergent ejector designed for a Mach number of 2.0 has been conducted at transonic speeds. Some preliminary results of the investigation are reported in reference 4. The present paper gives the off-design performance characteristics at transonic speeds of the fixed divergent ejector with secondary airflow and over a wider range of primary jet total-pressure ratios. Schlieren photographs of a small two-dimensional-flow visualization model of the ejector used in the wind-tunnel investigation are included.

The investigation was conducted at Mach numbers of 0.90, 0.95, 1.00, and 1.06 with the model angle of attack of  $0^\circ$  and with a jet total-pressure ratio from 1 (jet off) to 8. At each Mach number, secondary air weight flow was varied from zero to a value required to give a corrected weight-flow ratio of 0.04 or the maximum available with the air supply system at the higher jet pressure ratios. The fixed afterbody-nozzle arrangements were tested on a pylon-supported nacelle model with both nonafterburner and afterburner nozzles. The jet exhaust was simulated with a hydrogen peroxide hot-jet simulator as described in reference 5.

#### SYMBOLS

A            area, sq ft

$C_D$            drag coefficient,  $\frac{D}{q_\infty A_{\max}}$

$C_{D,a}$         afterbody pressure-drag coefficient,  $-\sum \frac{C_p A_l}{A_{\max}}$

$C_{F,ej}$        gross ejector jet thrust coefficient,  $\frac{F_{ej}}{q_\infty A_{\max}}$

CONFIDENTIAL

$C_p$	pressure coefficient, $\frac{p_l - p_\infty}{q_\infty}$
$D$	drag, lb
$d$	diameter, in.
$F$	jet thrust, lb
$F_{ej}$	ejector jet thrust, lb
$F_{i,p}$	ideal thrust for complete isentropic expansion of primary flow, $W \sqrt{\frac{2R}{g} \frac{\gamma}{\gamma - 1} T_{t,j} \left[ 1 - \left( \frac{p_\infty}{p_{t,j}} \right)^{\frac{\gamma-1}{\gamma}} \right]}$
$F_p$	primary-nozzle jet thrust, lb
$g$	gravitational acceleration, ft/sec <sup>2</sup>
$L$	ejector spacing, in.
$l$	axial distance from exit, positive forward, in.
$M$	free-stream Mach number
$m$	mass flow, slugs/sec
$p$	static pressure, lb/sq ft
$p_t$	total pressure, lb/sq ft
$p_{t,j}/p_\infty$	ratio of primary jet total pressure to free-stream static pressure
$q$	dynamic pressure, lb/sq ft
$r$	radius, in.
$R$	gas constant, ft/ <sup>o</sup> R
$T_t$	stagnation temperature, <sup>o</sup> R
$V$	velocity, ft/sec



W weight flow, lb/sec

$W_i$  ideal weight flow for choked exit,

$$p_{t,j} A_p \left( \frac{2}{\gamma + 1} \right)^{\frac{\gamma+1}{2(\gamma-1)}} \sqrt{\frac{\gamma g}{R T_{t,j}}}, \text{ lb/sec}$$

$\frac{W_s}{W_p} \sqrt{\frac{T_{t,s}}{T_{t,j}}}$  corrected secondary-to-primary weight-flow ratio

x longitudinal distance from reference point positive rearward, in.

y afterbody radial coordinate, in.

$\gamma$  ratio of specific heats

$\theta$  meridian angle, positive clockwise looking forward from afterbody exit, deg

Subscripts:

a afterbody

b base

bal balance

e exit of afterbody

ex external

f primary nozzle base

fore forebody

i ideal

j jet

l local

max maximum

p primary nozzle

UNCLASSIFIED

CONFIDENTIAL

5

s	seal, secondary
t	total, throat
$\infty$	free-stream conditions
1	forward compartment
2	outer compartment
3	inner compartment

## APPARATUS AND PROCEDURE

### Wind Tunnel

This investigation was conducted in the Langley 16-foot transonic tunnel, which is a single-return atmospheric wind tunnel, with an octagonal slotted test section. Tunnel Mach number can be varied from low subsonic values to about 1.08.

### Model and Support System

The pylon-supported-nacelle jet-simulator model described in reference 4 was used in the investigation. Figure 1 shows the model mounted in the tunnel test section and figure 2 is a sketch showing the dimensions and internal arrangement of the model and support system. The nacelle was attached to the pylon through a four-component internal strain-gage balance, and the hydrogen peroxide jet simulator which is described in reference 5 was attached to the pylon through a strain-gage thrust balance. This arrangement permitted the thrust and the nacelle forces and moments to be measured separately. As discussed in reference 6, the data for the pylon-supported model fairly represent a practical nacelle installation in spite of an unknown interference effect of the pylon. The jet simulator unit produces a hot-jet exhaust at a temperature of about 1,350° F.

### Ejector Configuration

The fixed divergent shroud ejector was designed for a flight Mach number of 2.0 and a jet pressure ratio of 10.1 with an afterburner primary nozzle and a corrected secondary weight-flow ratio of 0.042. The afterbody consisted of a curved boattail section with a small base. The

CONFIDENTIAL

primary nozzle only is varied to correspond to nonafterburning and afterburning conditions. A sketch of the combination of the fixed divergent shroud ejector and afterbody and the ejector parameters are shown in figure 3. The ejector geometry ratios, based on hot dimensions, are given in the following table:

	$d_e/d_p$	$d_t/d_p$	$d_b/d_p$	$L/d_p$	$L_t/d_p$	Divergence angle, deg
Nonafterburner	1.84	1.52	1.98	1.03	0.12	11
Afterburner	1.41	1.16	1.51	1.00	.30	11

### Tests

The model angle of attack was  $0^\circ$  throughout the Mach number range of 0.90 to 1.06. The average Reynolds number based on nacelle length was about  $20 \times 10^6$ . At each Mach number, the jet simulator system was operated at ratios of primary jet total pressure to free-stream static pressure from 1 (jet off) to maximum values of about 8 for several constant values of secondary air weight flow.

### Instrumentation

Primary jet thrust was obtained from the thrust balance, and the external axial forces on the nacelle were obtained from the internal balance. Pressures were measured on the afterbody, base, divergent ejector walls, and primary nozzle flap. Primary jet total pressure and temperature were measured in the tailpipe near the primary nozzle exit, and the secondary air total pressure and temperature were measured in the secondary air passage near the primary nozzle exit.

The primary weight flow was measured with a vane-type electronic flowmeter located in the hydrogen peroxide supply line. The secondary air weight flow was measured by using a sharp-edge orifice in the secondary air supply line.

### Data Reduction

The forces, pressures, and temperatures were converted to absolute values and standard coefficients by the process described in reference 3. The thrust balance measured the thrust of the primary nozzle and some internal forces. The drag element of the four-component balance measured

the external axial forces on the nacelle, the force on the divergent portion of the ejector, and some internal force. As shown in the appendix, the ejector thrust  $F_{ej}$  was obtained from the difference in balance readings plus the external drag of the model and an internal-pressure correction term:

$$F_{ej} = F_{bal} - D_{bal} + D_{fore} + D_a + (A_{s,2} - A_{s,1})(p_1 - p_2) + m_s V_s$$

The locations of the areas and pressures are shown in figure 4.

The secondary air weight flow was determined for each test point by using pressures measured at a sharp-edge orifice in the secondary air supply line along with measured stagnation temperature. Figure 5 shows the variation of the corrected secondary-to-primary weight-flow ratio with jet total-pressure ratio for all test Mach numbers at constant values of secondary air weight flow.

## Accuracy

The estimated accuracy of the data presented in this paper is as follows:

M . . . . .	±0.005
$p_{t,j}/p_\infty$ . . . . .	±0.10
$C_p$ . . . . .	±0.01
$C_{F,ej}$ . . . . .	±0.02
$\frac{w_s}{w_p} \sqrt{\frac{T_{t,s}}{T_{t,j}}}$ . . . . .	±0.005

## RESULTS AND DISCUSSION

### Pumping Characteristics

The variation of ejector total-pressure ratio  $p_{t,s}/p_{t,j}$  with primary jet total-pressure ratio for constant values of secondary air weight flow is shown in figure 6. Normally from these data plots it would be possible to determine the effect of secondary-passage total pressure on the amount of secondary airflow the ejector would pass. However, as seen in figure 6, the change in ejector total-pressure ratio at constant  $p_{t,j}/p_\infty$  for the range of secondary air weight flow of this investigation was small.

The flagged data points in figures 6(a) to 6(d) indicate data taken as the primary jet total-pressure ratio was decreased from a value required to attach the primary jet to the divergent portion of the ejector. The difference in the ejector total-pressure ratio for zero secondary air weight flow at primary jet total-pressure ratios around 4.0 is due to the different attachment characteristics (hysteresis) of the primary jet with increasing and decreasing primary jet total-pressure ratio.

### Pressure Distributions

Examples of pressure-coefficient variation over the afterbody, the primary nozzle base, and the divergent portions of the ejector are shown in figures 7 and 8 with the nonafterburning and the afterburning nozzles. Only the afterbody pressure coefficients at  $\theta = 0^\circ$  and the internal pressure coefficients at  $\theta = 10^\circ$  are shown. The data are presented for several values of Mach number and test values of primary jet total-pressure ratio and corrected weight-flow ratio. It should be noted that the test conditions at which the internal pressures are presented include those shown for the afterbody pressure distributions. Base pressure coefficients are included at  $l/d_e = 0$  (fig. 7) and  $l = 0$  inches (fig. 8).

With the exception of the data at zero secondary airflow and decreasing primary jet total-pressure ratio (flagged symbols, fig. 7(a)), the effect of the primary jet on the afterbody pressure coefficients was similar to results of investigations with parabolic afterbodies having large ratios of base diameter to primary jet diameter (for example, see ref. 7) and the effect of secondary air was small. For the excepted case, the afterbody pressures are more positive than for increasing primary jet total-pressure ratio. (For example, see data for  $M = 0.95$ ,  $\frac{W_s}{W_p} \sqrt{\frac{T_{t,s}}{T_{t,j}}} = 0$ , and  $p_{t,j}/p_\infty = 3.9$  in fig. 7(a).) The afterbody pressures can be affected by the jet shape and, with an ejector, hysteresis effects influence the jet shape in a rather complicated manner. For this configuration these effects resulted in more positive base pressures which, for the subsonic Mach numbers, were felt well forward on the afterbody.

For primary jet total-pressure ratios lower than 3.5 the internal wall pressures of the nonafterburning configuration (fig. 8(a)) are established by the base pressure. (See ref. 3.) As the primary jet total-pressure ratio is increased above 3.5 the internal pressures become more negative. They reach a minimum at a pressure ratio of about 6.0, and a further increase in primary jet total-pressure ratio then increases

the level of the pressures. (For example, see data in fig. 8(a) for  $M = 1.06$  and  $\frac{W_s}{W_p} \sqrt{\frac{T_{t,s}}{T_{t,j}}} = 0.029$ .)

The variation of the internal pressure distributions for the afterburning configuration is seen in figure 8(b). The internal pressures are affected at a much lower primary jet total-pressure ratio than for the nonafterburning configuration. The pressure orifice located at  $l = 1.96$  is in the ejector throat and in general indicates jet impingement. Because of the jet impingement between  $l = 1.96$  and  $l = 2.85$ , it is felt that the fairing of the curves between these two points does not necessarily indicate the true pressure variation between the two points. For the lower primary jet total-pressure ratios of the investigation, downstream from the ejector throat the pressures along the ejector wall become more negative, then more positive, indicating attachment and overexpansion of the primary jet. Increasing the primary jet total-pressure ratio to about 8.0 produces positive pressures over most of the ejector. At the higher pressure ratios the pressures over the divergent portion of the ejector were little affected by the amounts of secondary air used in this investigation; however, there was a large effect of secondary air on the pressures over the primary nozzle base.

The internal pressure distribution for the afterburning configuration (fig. 8(b)) indicates jet impingement in the region of the ejector throat at lower primary jet total-pressure ratios than would be expected. It was believed that the rounded shape of the primary nozzle exit changed the initial shape of the jet boundary. In order to obtain an idea of the effect of the primary-nozzle-exit lip shape on the shape of the primary jet boundary, a small two-dimensional-flow visualization model of the ejector used in the tunnel investigation was constructed and schlieren photographs were taken as the primary jet total-pressure ratio was varied. The nonafterburning primary nozzle used in the tunnel investigation had a short straight section at the exit and the afterburning primary nozzle had a rounded exit lip. (See fig. 3.) The photographs in figure 9 compare the jet boundary shapes from such nozzle exits with those from nozzles having sharp-edge exits. There was little difference in the results for the nonafterburning configurations (fig. 9(a)), but rounding the afterburning nozzle caused the jet to turn out and impinge (fig. 9(b)). The results shown in figure 9 indicate that the primary-nozzle lip shape can greatly change the initial jet profile.

### Drag Characteristics

The variation of the afterbody drag coefficient with primary jet total-pressure ratio at constant values of corrected weight-flow ratio for each of the test Mach numbers is shown in figure 10. The afterbody

drag coefficient includes the base drag and was obtained by integration of the measured pressures over the afterbody and base. The effect of the primary jet and of the corrected secondary weight-flow ratio on the afterbody drag was small. The variation of the external and forebody drag coefficients with Mach number is shown in figure 11 for zero secondary air and jet-off conditions.

### Primary Jet Nozzle Performance

Two measures of the primary jet nozzle performance are the flow coefficient or ratio of the measured weight flow to the ideal weight flow based on the measured jet total pressures and temperatures, and the thrust coefficient or ratio of the measured jet thrust to the ideal primary thrust based on measured primary weight flow and jet total pressures and temperatures. The variations of the primary nozzle flow and thrust coefficients with primary jet total-pressure ratio are shown in figure 12 and are consistent with expected values (ref. 5).

### Gross Ejector Thrust

The effect of primary jet total-pressure ratio and secondary air weight flow on the gross ejector thrust coefficient is shown in figure 13 for the nonafterburning and the afterburning nozzles at constant Mach numbers. For the nonafterburning configuration, data were taken at increasing and decreasing primary jet total-pressure ratios. The data, obtained as the primary jet total-pressure ratio was decreased from a value above that required for jet attachment to the divergent wall, are indicated by flagged symbols. The solid symbols indicate additional data that were obtained from the continuous record between test points. As a result of the difference in the response of the primary jet total-pressure gage and the force-balance readout systems, the ejector thrust coefficient for these points is slightly high for decreasing primary jet total-pressure ratio.

Nonafterburning. - The variation of ejector thrust coefficient with primary jet total-pressure ratio is shown for the nonafterburning configuration in figures 13(a) to 13(d). As the primary jet total-pressure ratio is increased from jet off to about 4.0, the pressure distributions in the divergent portion of the ejector are little affected by the primary jet, but, as seen in figure 8, are of the order of the base pressure. However, as the jet boundary approaches the wall of the ejector, the pressure in the secondary passage is reduced by jet pumping which causes the jet to enlarge initially and attach to the ejector wall. The loss in ejector thrust which occurs between primary jet total-pressure ratios of 4.0 and 4.5 for low values of secondary air is a result of the negative pressures along the ejector wall. Increasing the secondary air

reduces the thrust loss as well as delays it to a higher primary jet total-pressure ratio.

As shown by the flagged symbols in figures 13(a) to 13(d), the primary jet remains attached to the ejector wall to a lower primary jet total-pressure ratio, and thereby produces larger losses in ejector thrust than those for increasing primary jet total-pressure ratio. For this ejector configuration the addition of about 2 percent secondary air will prevent this extreme overexpansion as the primary jet total-pressure ratio is decreased. This primary jet attachment hysteresis has also been seen in the results of other investigations. (For example, see ref. 8.)

Afterburning.- The variation of the ejector thrust coefficient with the primary jet total-pressure ratio is shown for the afterburning configuration in figures 13(e) to 13(h). It can be seen that the ejector thrust coefficient increased with the primary jet total-pressure ratio without the sudden losses which occurred with the nonafterburning configuration. However, as stated previously, jet attachment to the ejector wall occurred at a much lower primary jet total-pressure ratio than for the nonafterburning configuration, and as seen in the pressure distributions (fig. 8) the flow was overexpanded to such an extent that the jet impinged upstream of the ejector minimum. The impingement of the primary jet upstream of the ejector minimum resulted in large losses in ejector thrust over the range of primary jet total-pressure ratio of the investigation.

## Ejector Performance

The ratios of ejector thrust to ideal primary thrust are presented in figure 14 at constant values of corrected weight-flow ratio for each of the test Mach numbers. The effect of corrected weight-flow ratio on the ejector thrust ratio varied somewhat erratically with Mach number and primary jet total-pressure ratio. Generally, for the nonafterburning configuration, below a primary jet total-pressure ratio of about 3.5 the addition of secondary air had little or slight detrimental effect on performance and at the higher pressure ratios the larger amounts of secondary air usually caused an increase in ejector thrust ratio. The effect of secondary airflow on the afterburner-configuration ejector thrust ratio was generally small except at the lowest pressure ratios.

In order to indicate the losses associated with the off-design performance of the ejectors, the variation of the ejector thrust ratio with Mach number is presented in figure 15 at scheduled values of corrected weight-flow ratio and primary jet total-pressure ratio. The variation of primary jet total-pressure ratio and corrected weight-flow ratio with Mach number is also shown in figure 15 and is considered typical of current



operating turbojet-engine installations. It is obvious that, while satisfactory nonafterburning operation is possible from  $M = 0.90$  to  $M = 1.01$ , there will be large losses above  $M = 1.01$  for the nonafterburning configuration and that the performance of the afterburning configuration is poor for the Mach number range of the investigation. As shown previously, these losses are due to overexpansion of the primary jet.

#### CONCLUDING REMARKS

An investigation of a pylon-supported nacelle model with a fixed divergent ejector designed for a Mach number of 2.0 has been conducted in the Langley 16-foot transonic tunnel over a Mach number range from 0.90 to 1.06. The results of the investigation warrant the following remarks:

1. The performance of the nonafterburner nozzle configuration at scheduled conditions was satisfactory up to a Mach number of 1.00.
2. The addition of about 2 percent secondary air eliminated the primary jet attachment hysteresis with the nonafterburner nozzle.
3. The afterburner-nozzle configuration experienced large losses due to primary jet overexpansion over the Mach number range of the investigation at scheduled operating conditions.
4. The initial shape of the primary jet boundary and thereby the ejector performance can be greatly affected by the shape of the primary-nozzle exit lip.

Langley Research Center,  
National Aeronautics and Space Administration,  
Langley Field, Va., August 12, 1959.

## APPENDIX

### METHOD OF CALCULATION

#### Drag System

The drag component of the main balance measured the axial forces on the external surface of the nacelle and inside the afterbody to the center of the rear seal of the model (see fig. 4), as well as an internal pressure force. The equation for the external drag of the model is as follows:

$$D_{ex} = D_{bal} + (p_1 - p_{\infty})A_{s,1} + (p_2 - p_{\infty})(A_{s,2} - A_{s,1}) - (p_f - p_{\infty})(A_{s,2} - A_s) + \int_{A_s}^{A_t} (p_l - p_{\infty})dA + \int_{A_t}^{A_e} (p_l - p_{\infty})dA \quad (1)$$

Because static calibrations indicated that for this investigation the internal friction forces due to the secondary air were small, they are neglected in the equation for  $D_{ex}$ . The internal friction force due to the primary jet flow on the divergent ejector surface, which is measured by the drag balance, is also neglected. The external drag is defined as the sum of all the axial forces acting on the external surface of the model, including the base (that is, the forebody plus the afterbody drag). Therefore, the forebody drag is as follows:

$$D_{fore} = D_{ex} - D_a \quad (2)$$

The forebody drag varied only with Mach number and was determined from jet-off tests. The afterbody drag does not include the friction drag; therefore, the forebody drag obtained using equation (2) is actually the drag of the forebody plus the friction drag of the afterbody.

#### Thrust System

The thrust balance measured the primary thrust plus some internal forces including the thrust of the incoming secondary air. Static calibrations with the primary jet off indicated that the thrust of the

incoming secondary air and the friction forces in the secondary passage were small and for this investigation could be neglected. Therefore the thrust of the primary nozzle is

$$F_p = F_{bal} + (p_1 - p_\infty)A_{s,2} - (p_f - p_\infty)(A_{s,2} - A_p) \quad (3)$$

The locations of the balance, areas, and pressures are shown in figure 4.

#### Ejector Thrust

The thrust of an ejector is the sum of the primary thrust, the secondary thrust at the plane of the primary nozzle exit, and the sum of the pressure and viscous forces acting on the wall of the ejector downstream from the primary nozzle exit. If the viscous force acting on the ejector wall is neglected, the expression for ejector thrust is

$$F_{ej} = F_{bal} + (p_1 - p_\infty)A_{s,2} - (p_f - p_\infty)(A_{s,2} - A_p) + m_s V_s + (p_f - p_\infty)(A_s - A_p) + \int_{A_s}^{A_t} (p_l - p_\infty) dA + \int_{A_t}^{A_e} (p_l - p_\infty) dA \quad (4)$$

The propulsive force can now be obtained by taking the difference of the ejector thrust force and the external drag force.

$$F_{ej} - D_{ex} = F_{bal} - D_{bal} + (p_1 - p_2)(A_{s,2} - A_{s,1}) + m_s V_s \quad (5)$$

Then, since

$$D_{ex} = D_{fore} + D_a$$

the ejector thrust is

$$F_{ej} = F_{bal} - D_{bal} + (p_1 - p_2)(A_{s,2} - A_{s,1}) + m_s V_s + D_{fore} + D_a \quad (6)$$

## REFERENCES

1. Greathouse, William K., and Beale, William T.: Performance Characteristics of Several Divergent-Shroud Aircraft Ejectors. NACA RM E55G21a, 1955.
2. Trout, Arthur M., Papell, S. Stephen, and Povolny, John H.: Internal Performance of Several Divergent-Shroud Ejector Nozzles With High Divergence Angles. NACA RM E57F13, 1957.
3. Swihart, John M., and Mercer, Charles E.: Investigation at Transonic Speeds of a Fixed Divergent Ejector Installed in a Single-Engine Fighter Model. NACA RM L57L10a, 1958.
4. Runckel, Jack F.: Preliminary Transonic Performance Results for Solid and Slotted Turbojet Nacelle Afterbodies Incorporating Fixed Divergent Jet Nozzles Designed for Supersonic Operation. NASA MEMO 10-24-58L, 1958.
5. Runckel, Jack F., and Swihart, John M.: A Hydrogen Peroxide Hot-Jet Simulator for Wind-Tunnel Tests of Turbojet-Exit Models. NASA MEMO 1-10-59L, 1959.
6. Swihart, John M., Mercer, Charles E., and Norton, Harry T., Jr.: Effect of Afterbody-Ejector Configurations on the Performance at Transonic Speeds of a Pylon-Supported Nacelle Model Having a Hot-Jet Exhaust. NASA MEMO 1-4-59L, 1959.
7. Englert, Gerald W., Vargo, Donald J., and Cubbison, Robert W.: Effect of Jet-Nozzle-Expansion Ratio on Drag of Parabolic Afterbodies. NACA RM E54B12, 1954.
8. Kochendorfer, Fred D., and Rousso, Morris D.: Performance Characteristics of Aircraft Cooling Ejectors Having Short Cylindrical Shrouds. NACA RM E51E01, 1951.



L-57-2316  
Figure 1.- Photograph of pylon-supported nacelle model with fixed divergent-ejector  
afterbody installed in the 16-foot transonic tunnel.

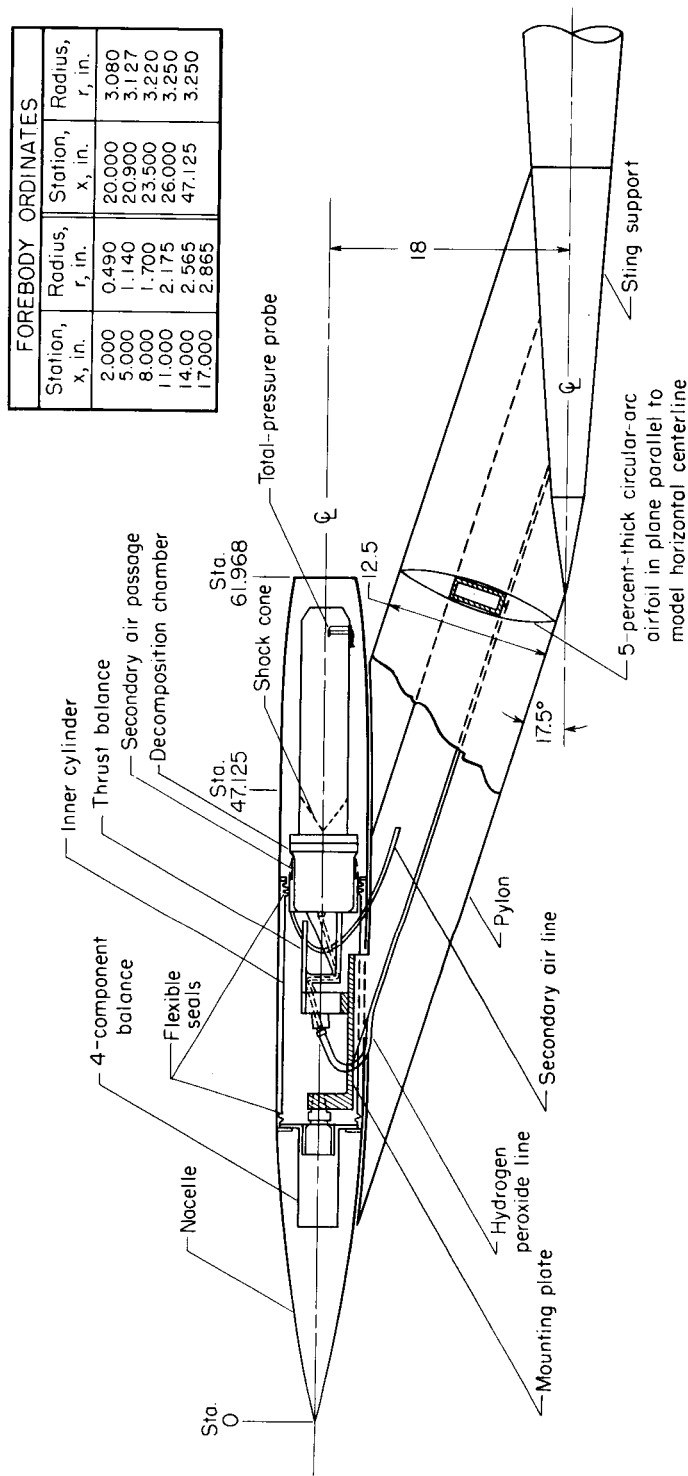


Figure 2.- Sketch of pylon-supported nacelle model. All dimensions are in inches.

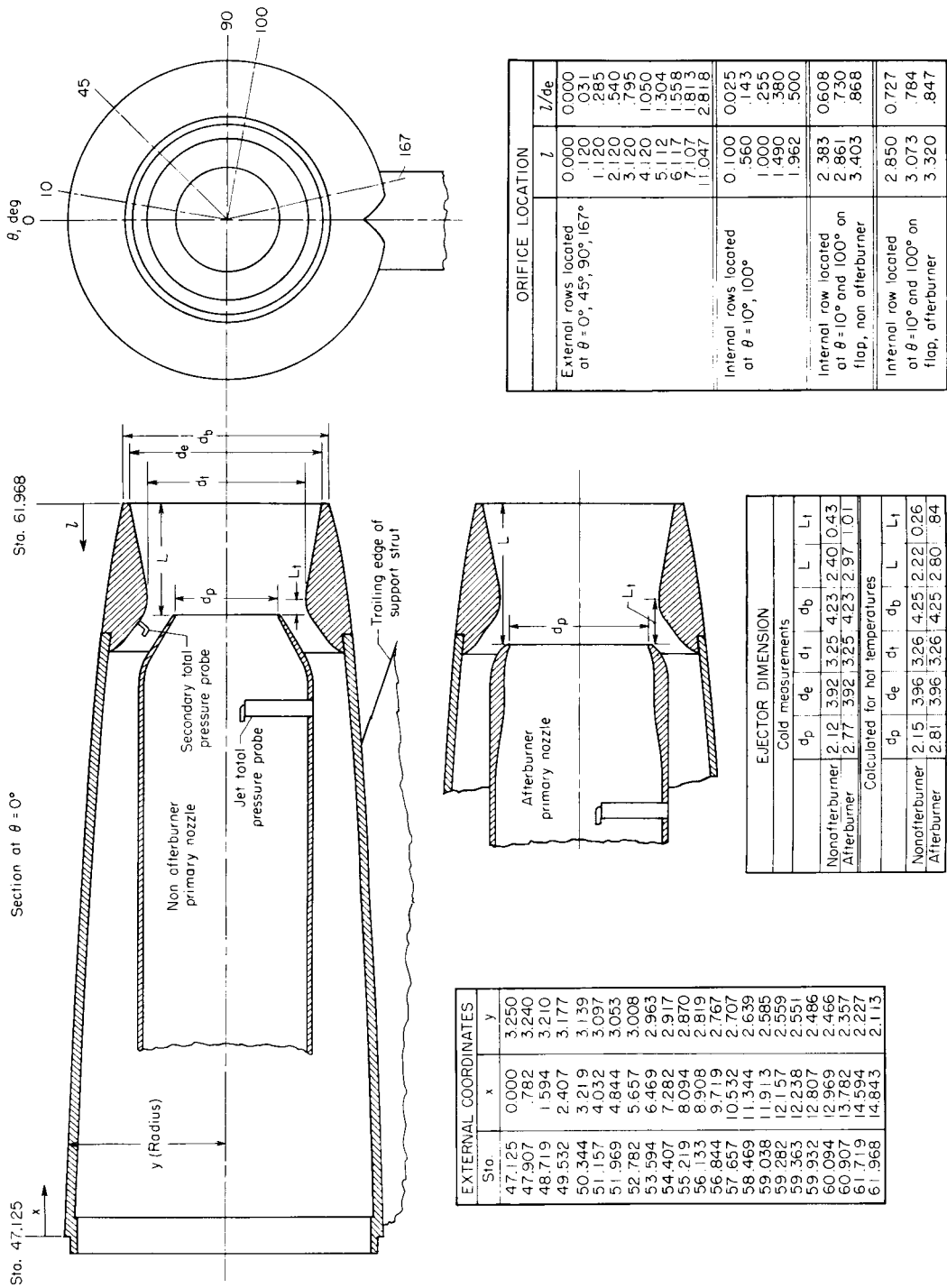


Figure 3.- Sketch of combination of fixed divergent shroud ejector and afterbody.  
All dimensions are in inches.

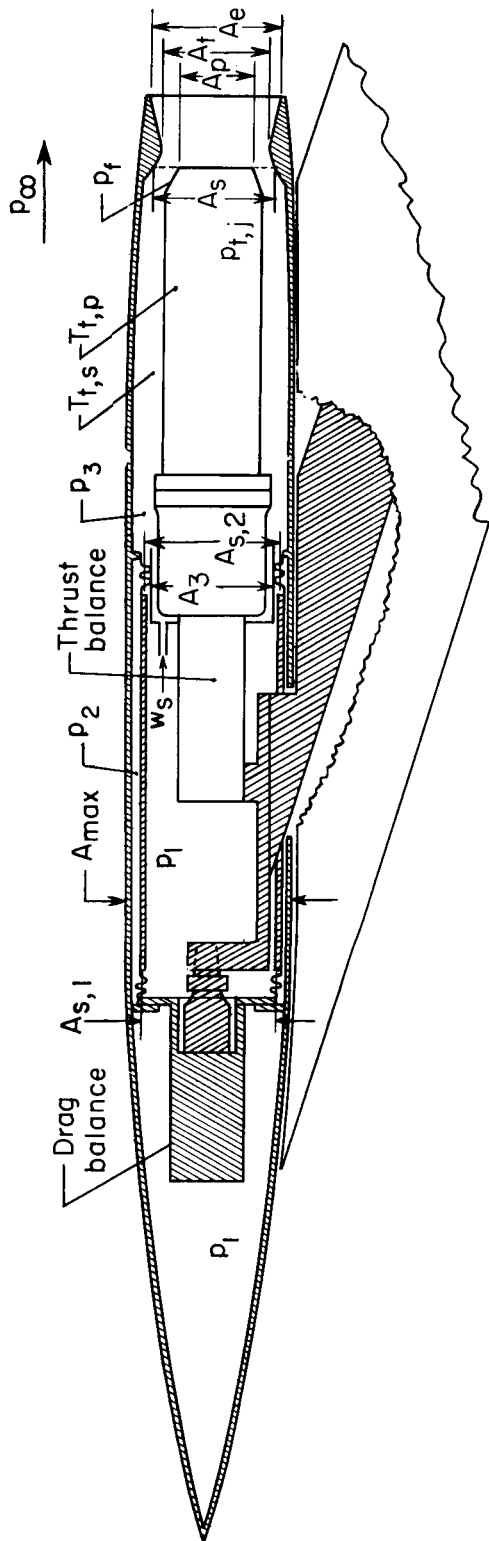
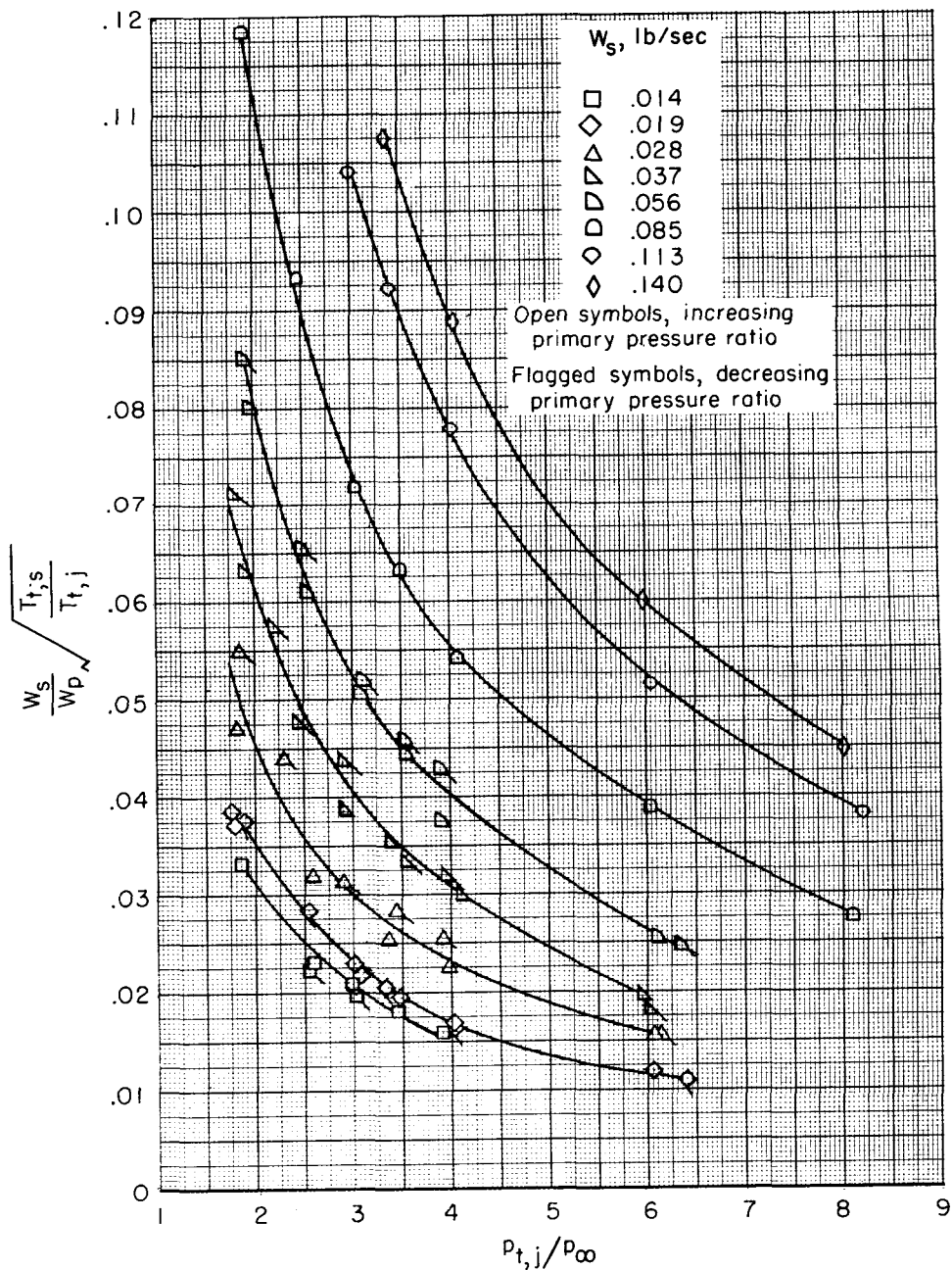


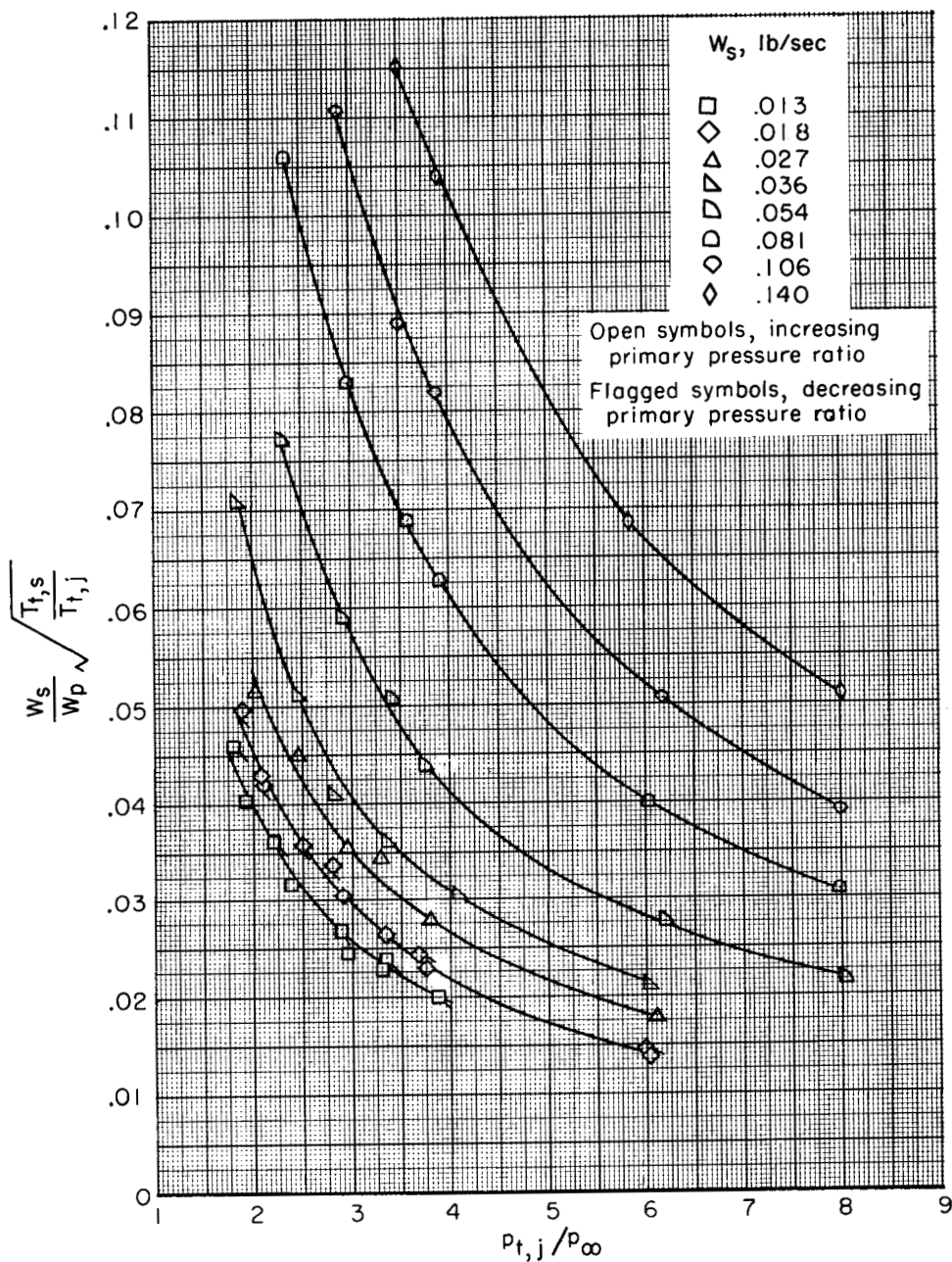
Figure 4.- Schematic diagram showing thrust and drag systems.





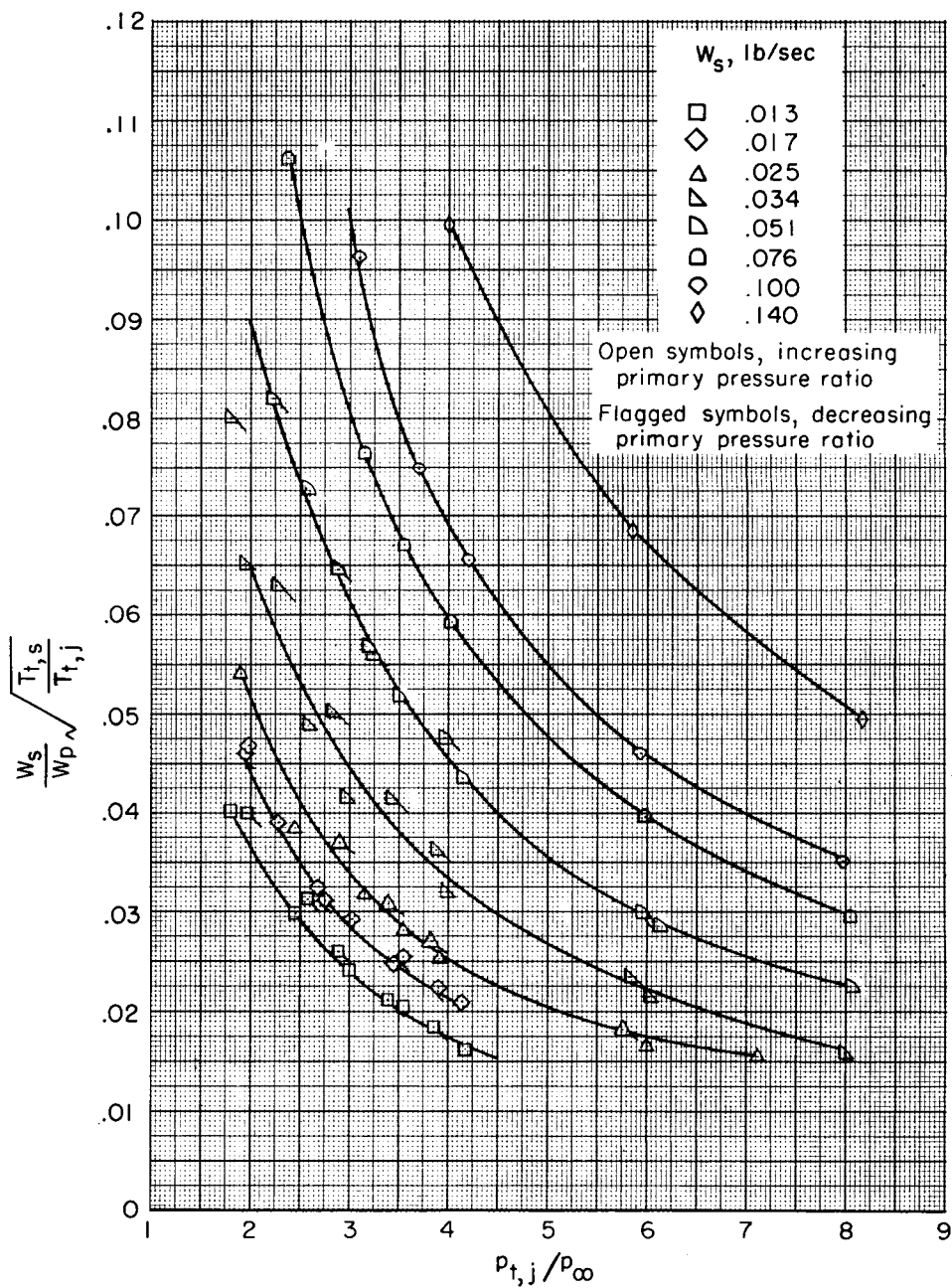
(a)  $M = 0.90$ ; nonafterburning nozzle.

Figure 5.- Variation of corrected weight-flow ratio with primary pressure ratio at constant values of secondary air weight flow.



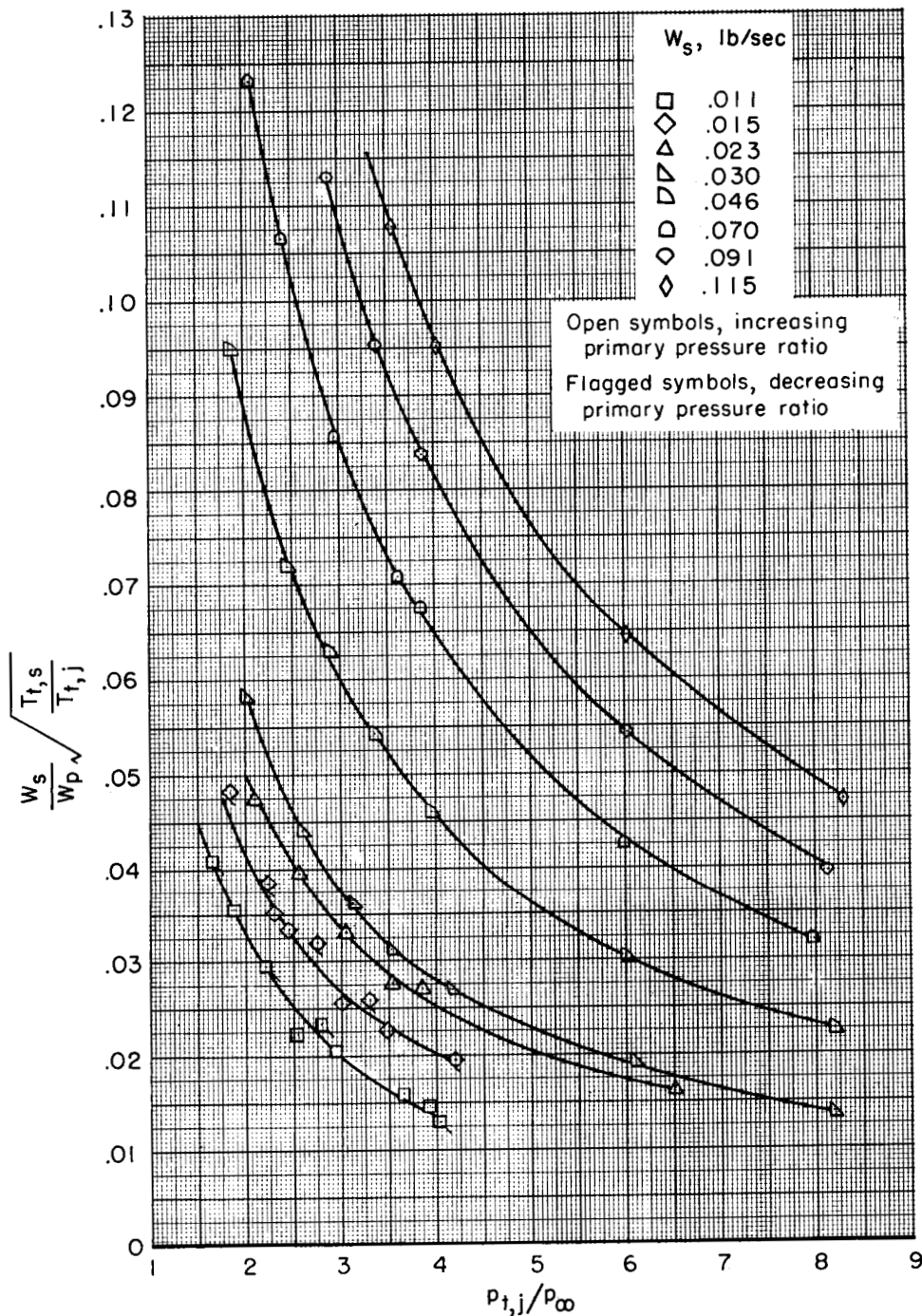
(b)  $M = 0.95$ ; nonafterburning nozzle.

Figure 5.- Continued.



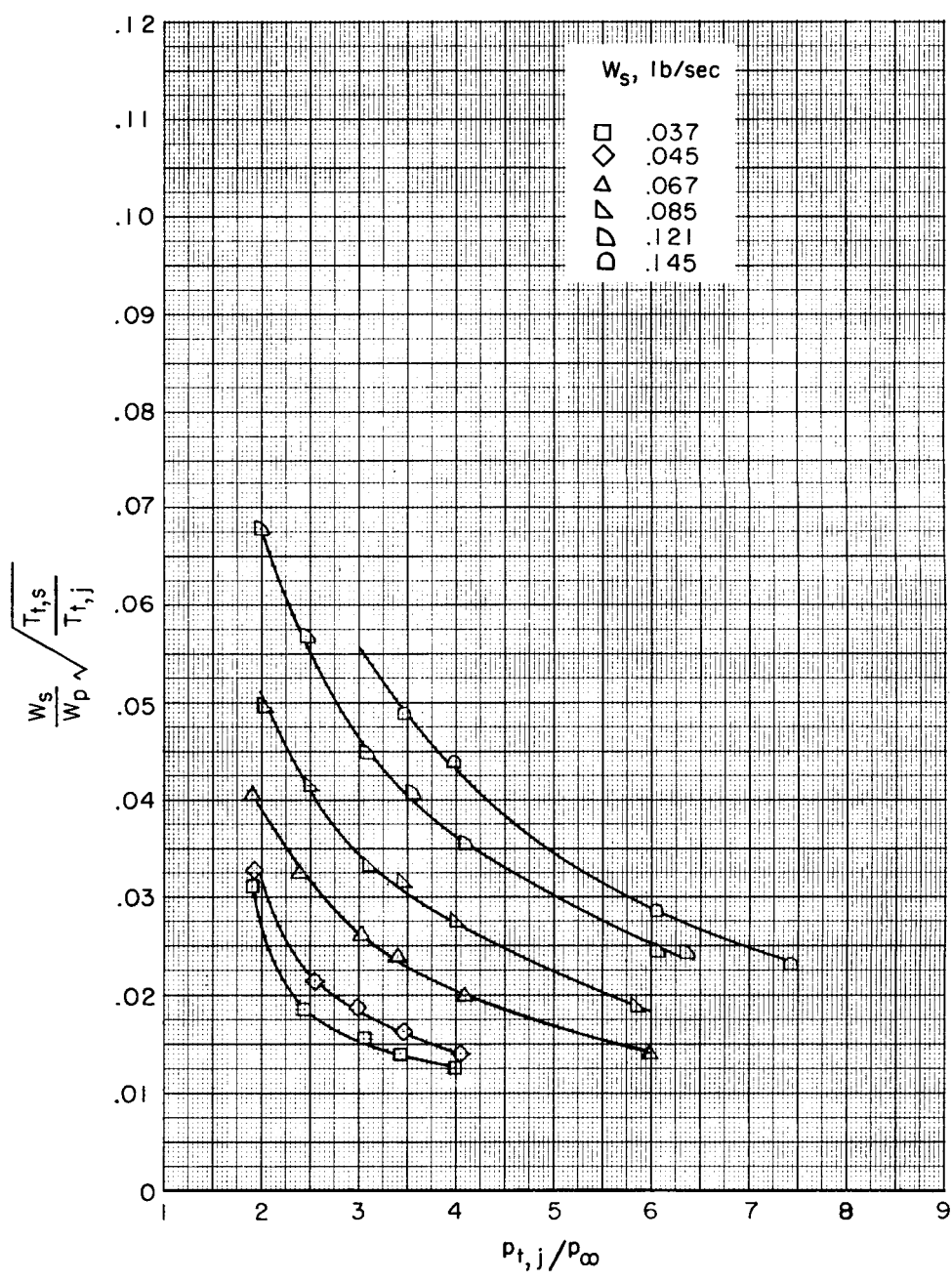
(c)  $M = 1.00$ ; nonafterburning nozzle.

Figure 5.- Continued.



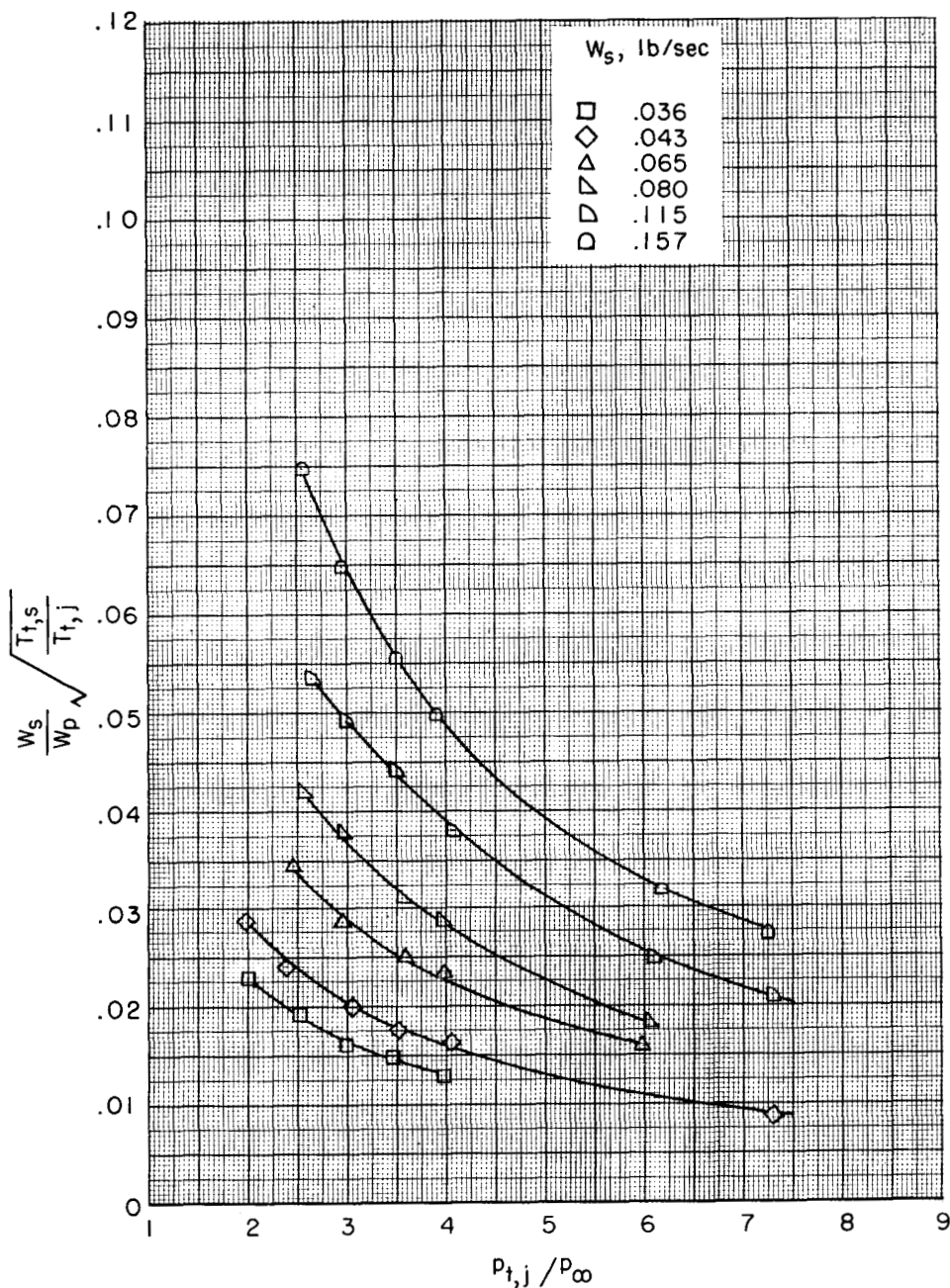
(d)  $M = 1.06$ ; nonafterburning nozzle.

Figure 5.- Continued.



(e)  $M = 0.90$ ; afterburning nozzle.

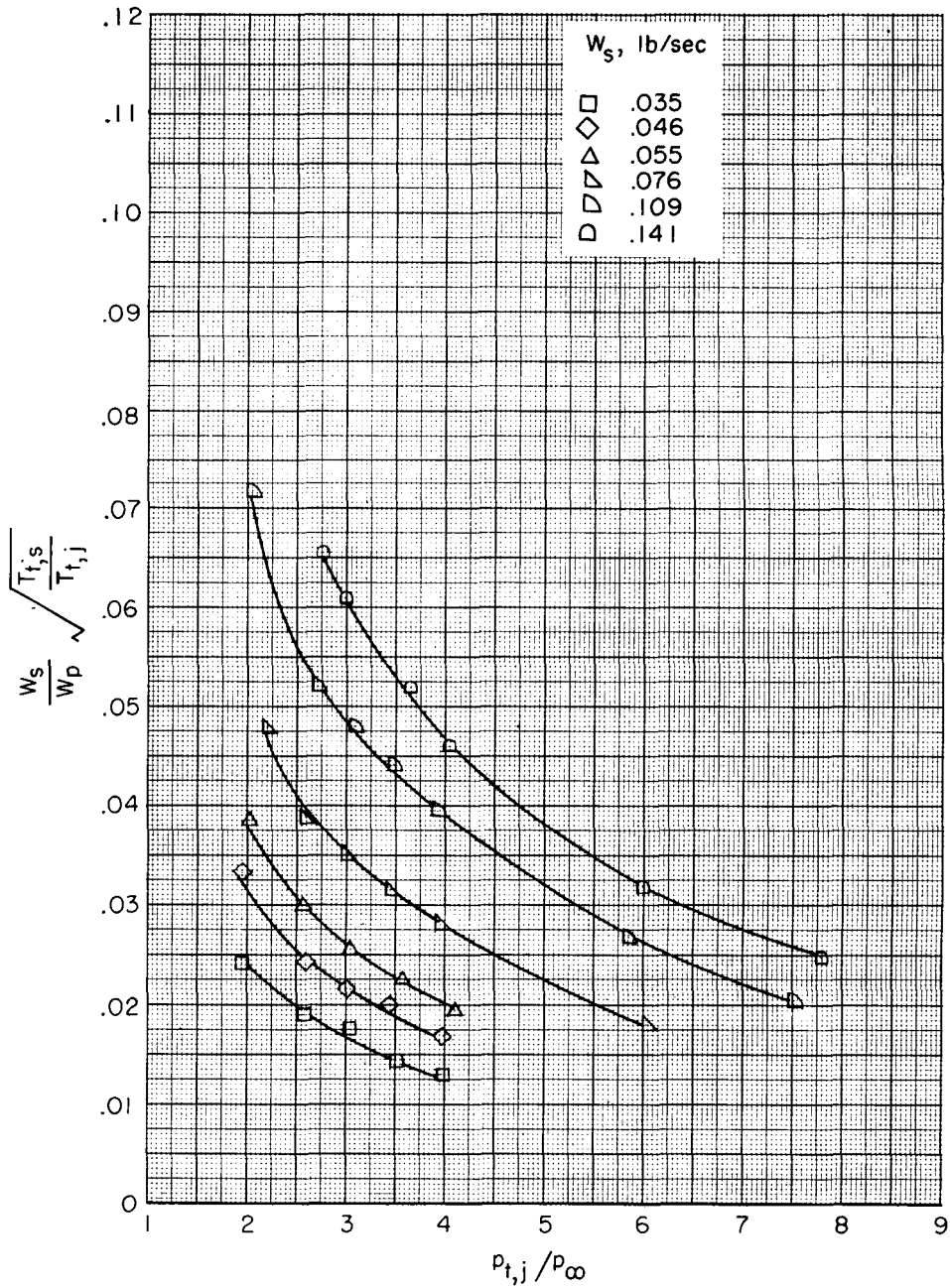
Figure 5.- Continued.



(f)  $M = 0.95$ ; afterburning nozzle.

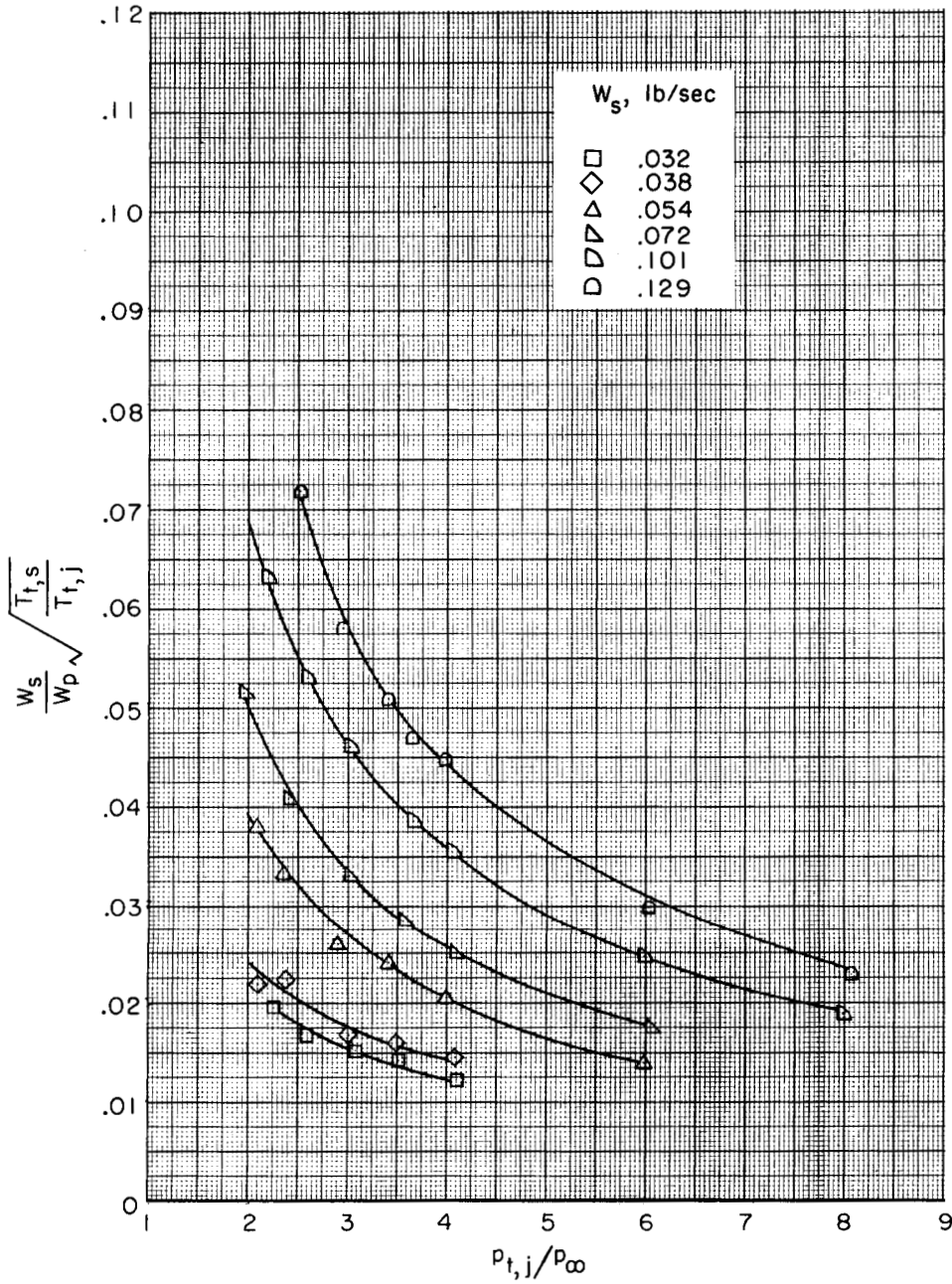
Figure 5.- Continued.





(g)  $M = 1.00$ ; afterburning nozzle.

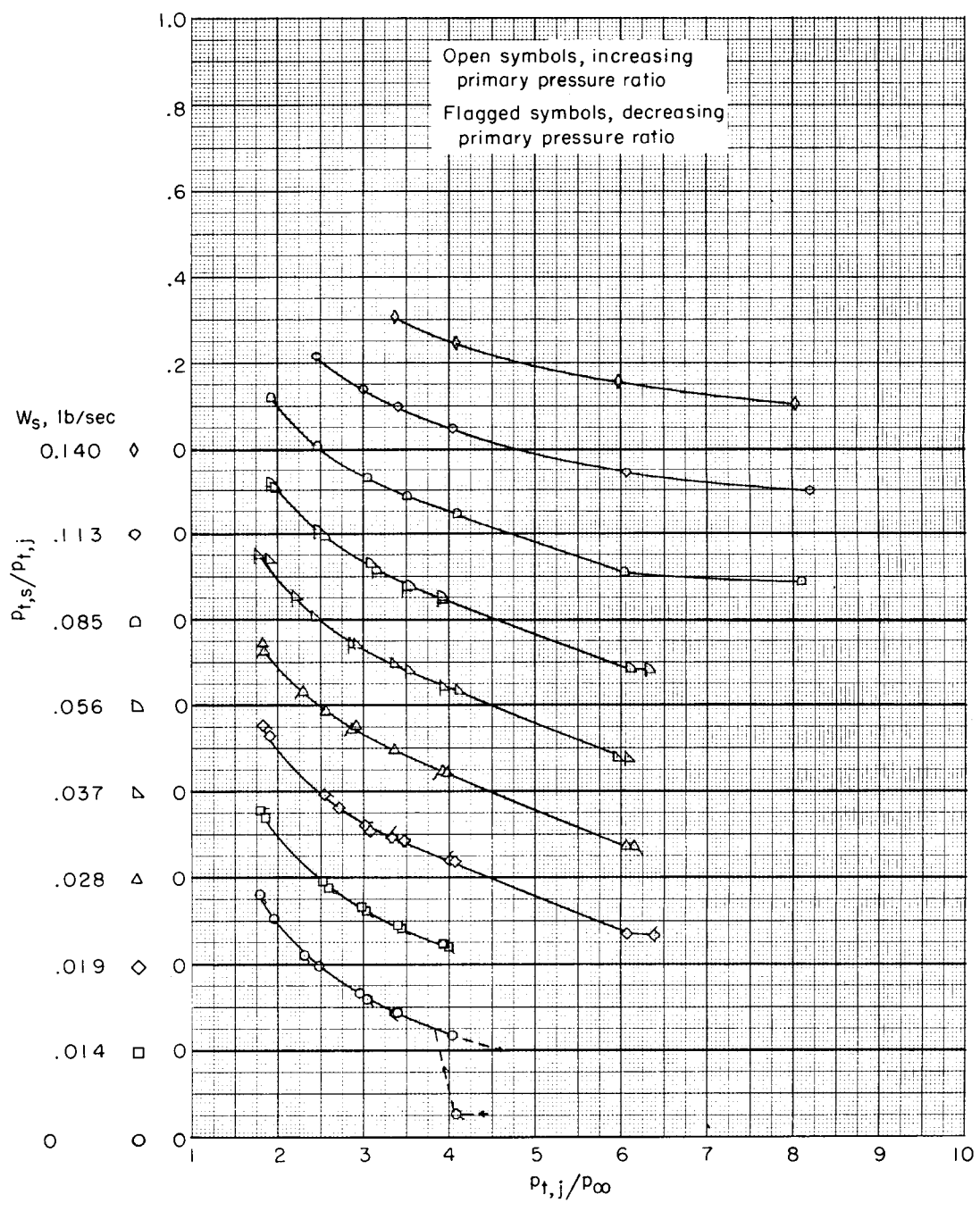
Figure 5.- Continued.



(h)  $M = 1.06$ ; afterburning nozzle.

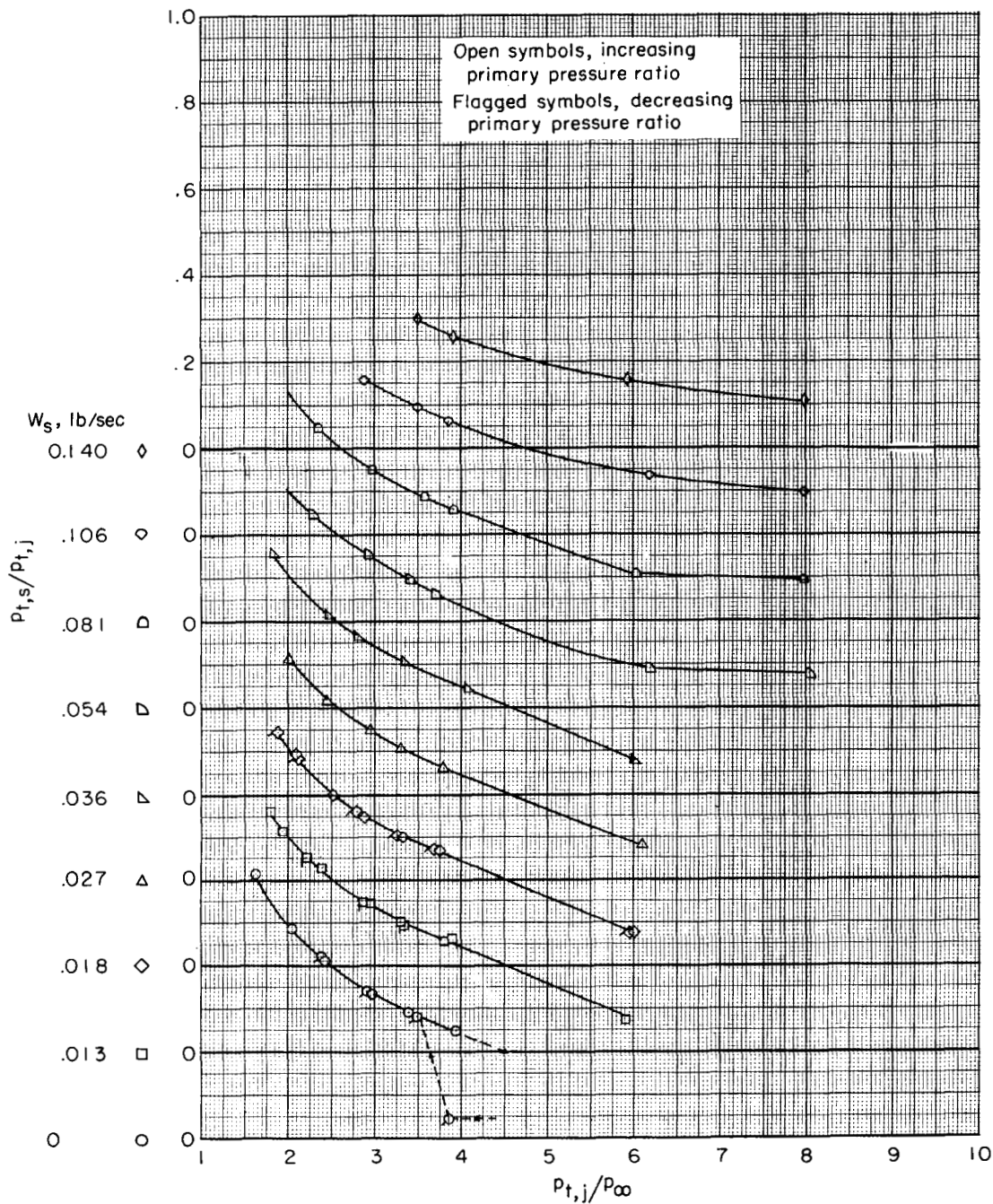
Figure 5.- Concluded.





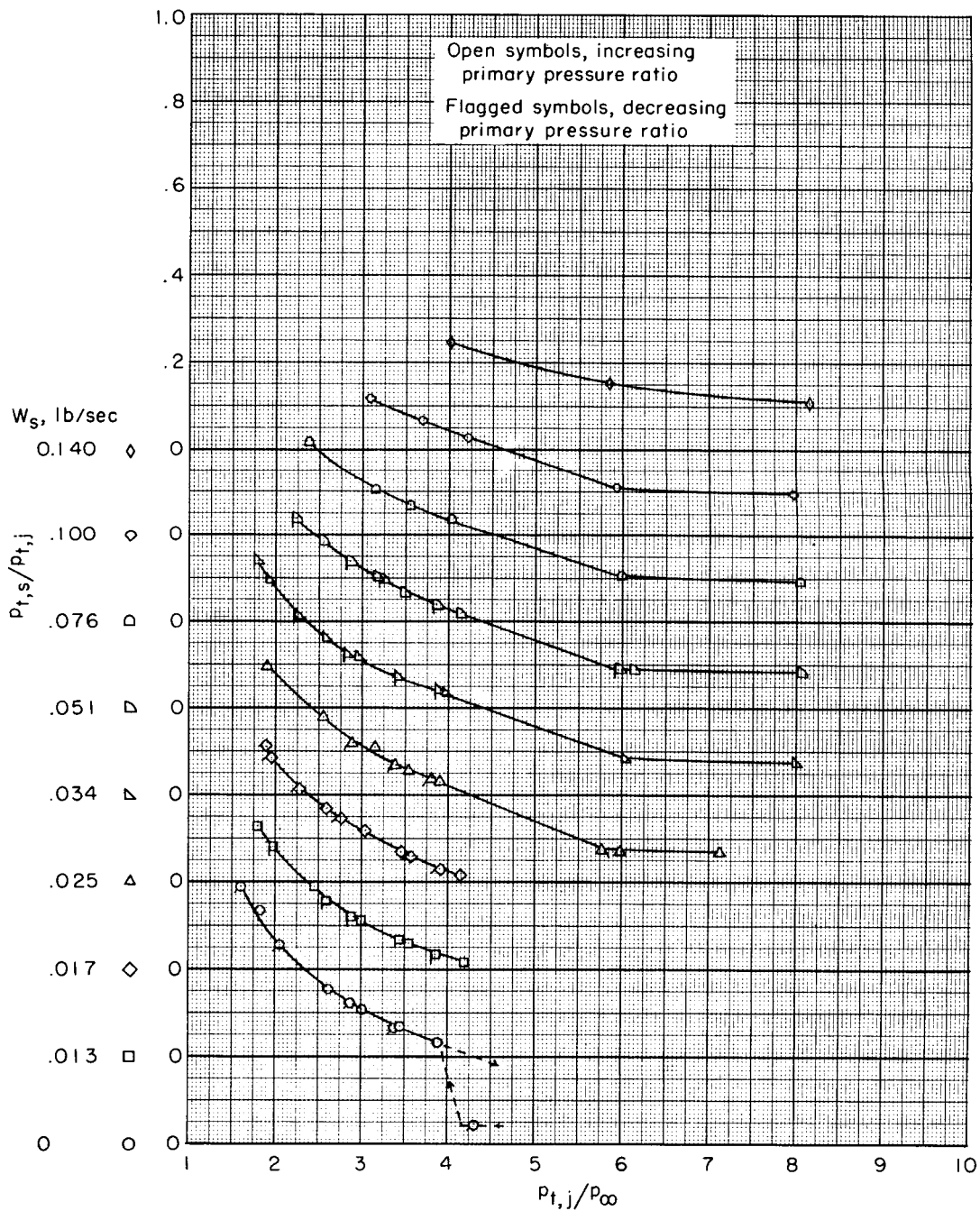
(a)  $M = 0.90$ ; nonafterburning nozzle.

Figure 6.- Variation of ejector flow characteristics with primary pressure ratio at constant values of secondary air weight flow.



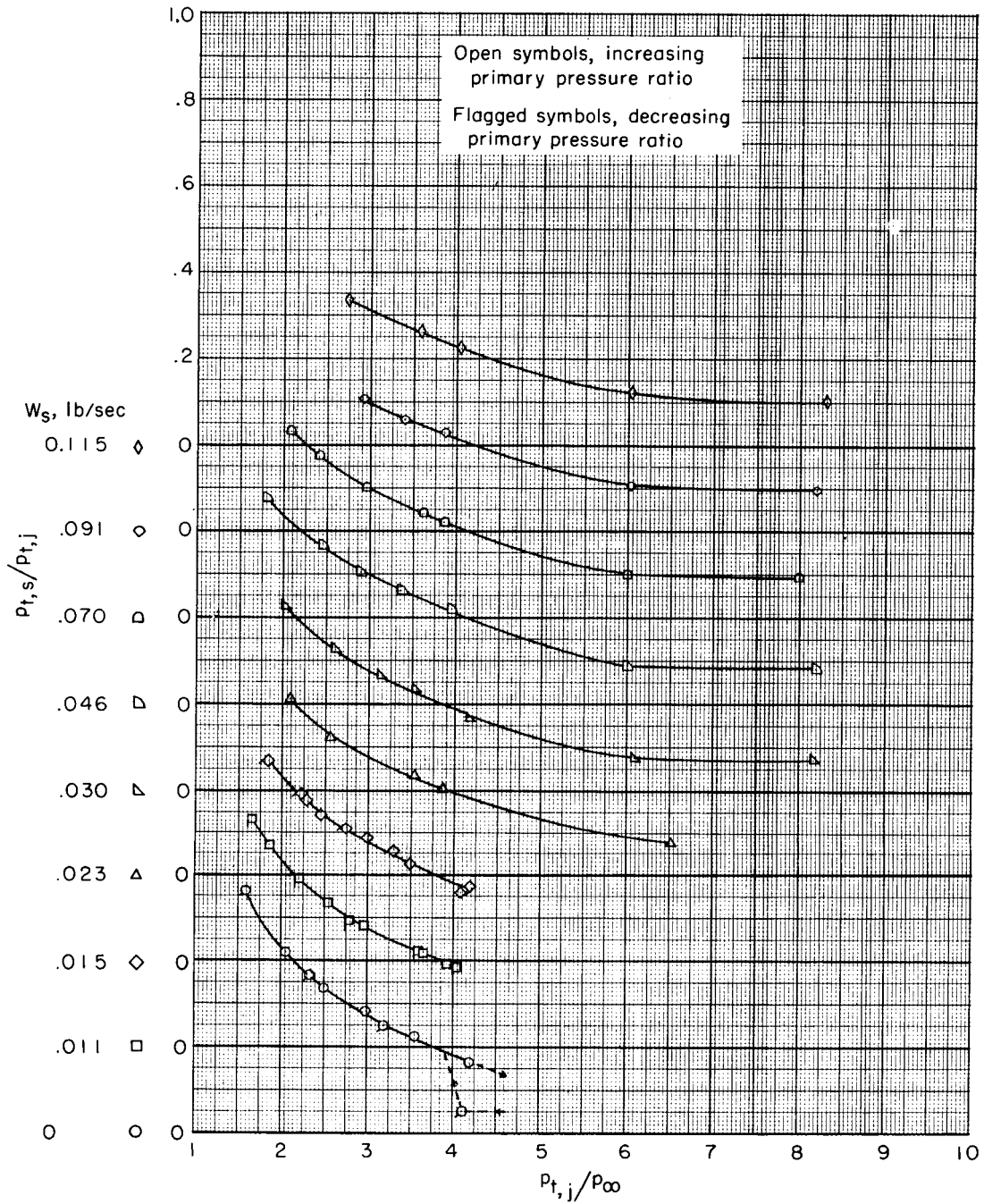
(b)  $M = 0.95$ ; nonafterburning nozzle.

Figure 6.- Continued.



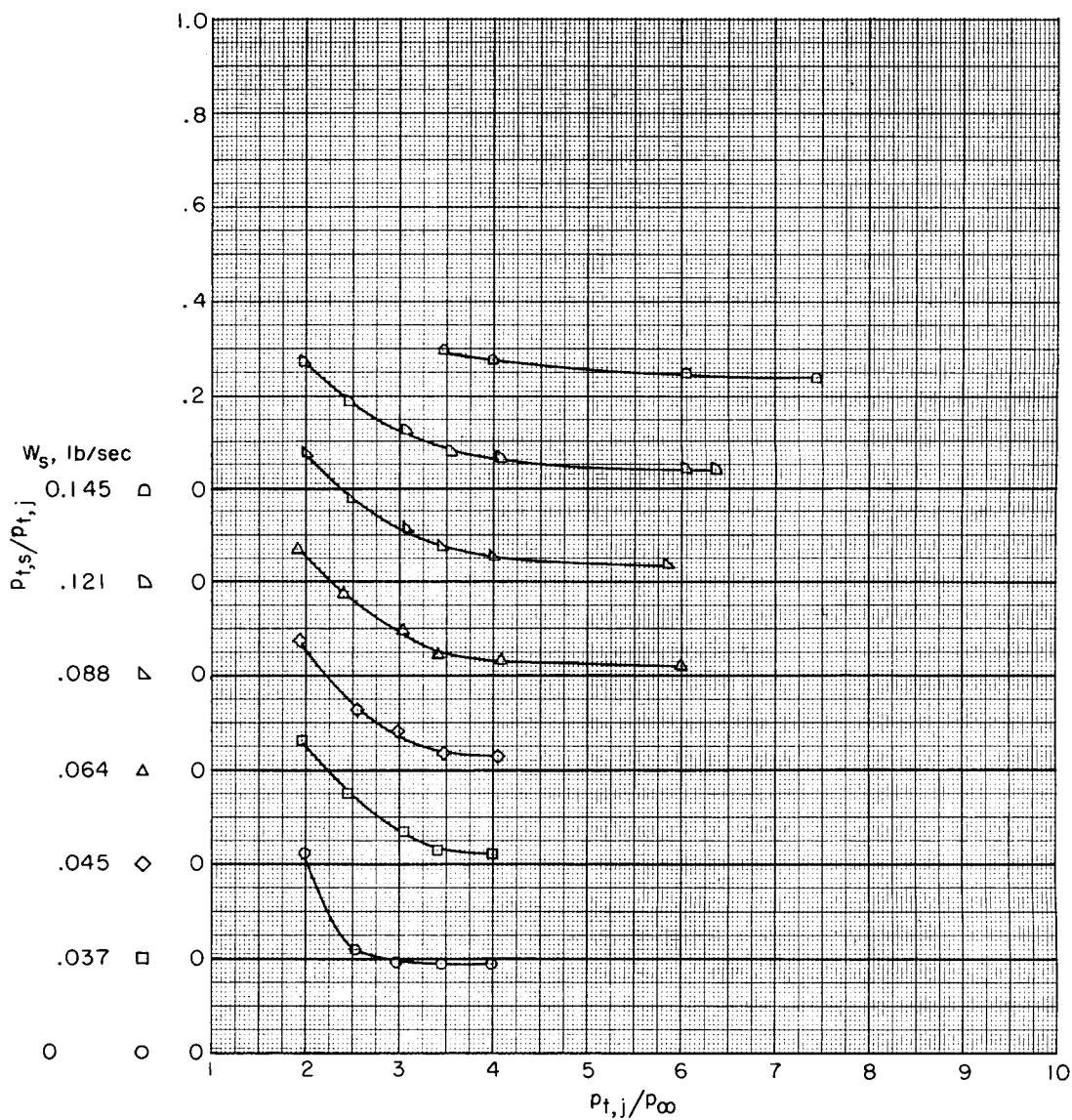
(c)  $M = 1.00$ ; nonafterburning nozzle.

Figure 6.- Continued.



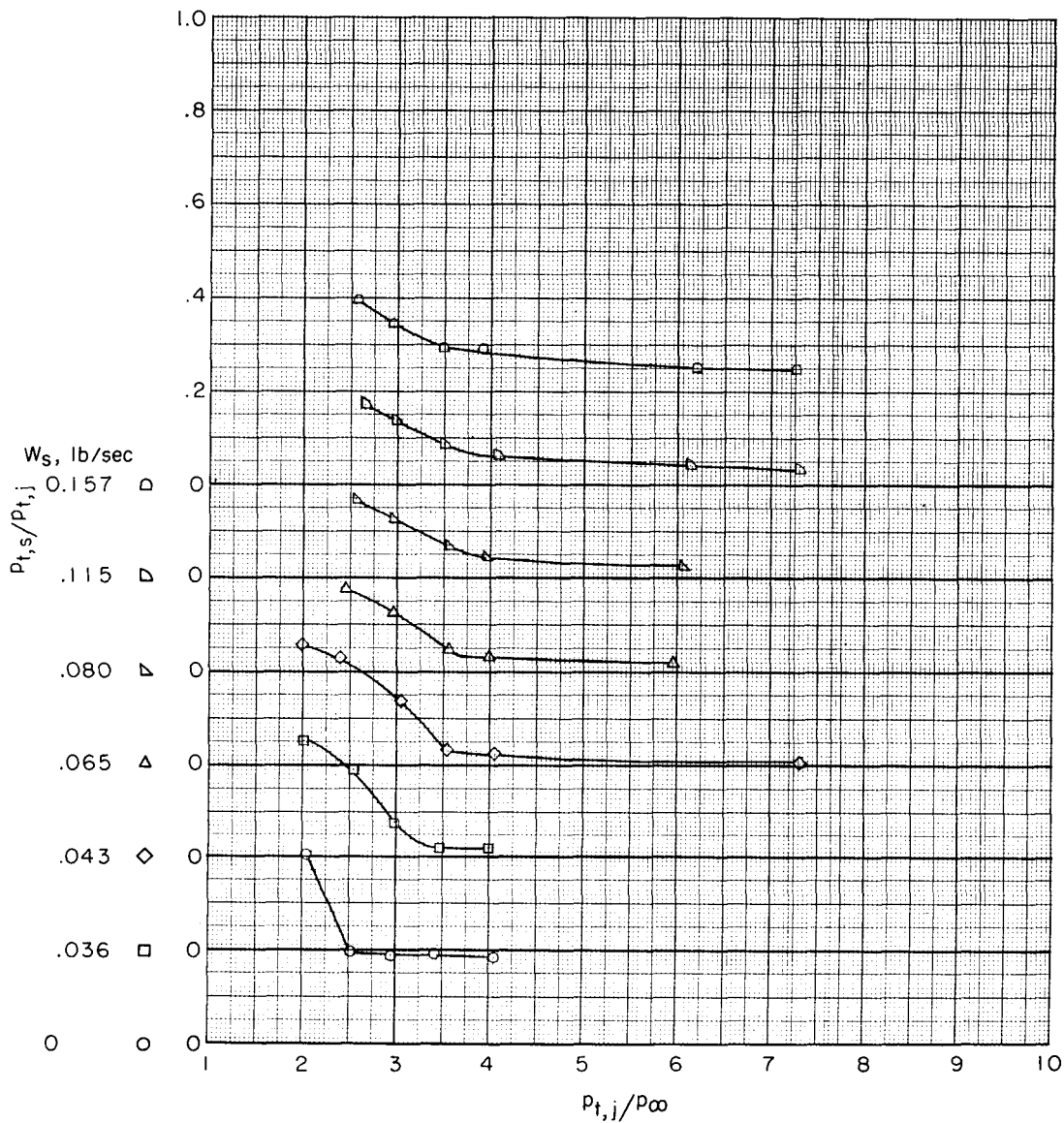
(d)  $M = 1.06$ ; nonafterburning nozzle.

Figure 6.- Continued.



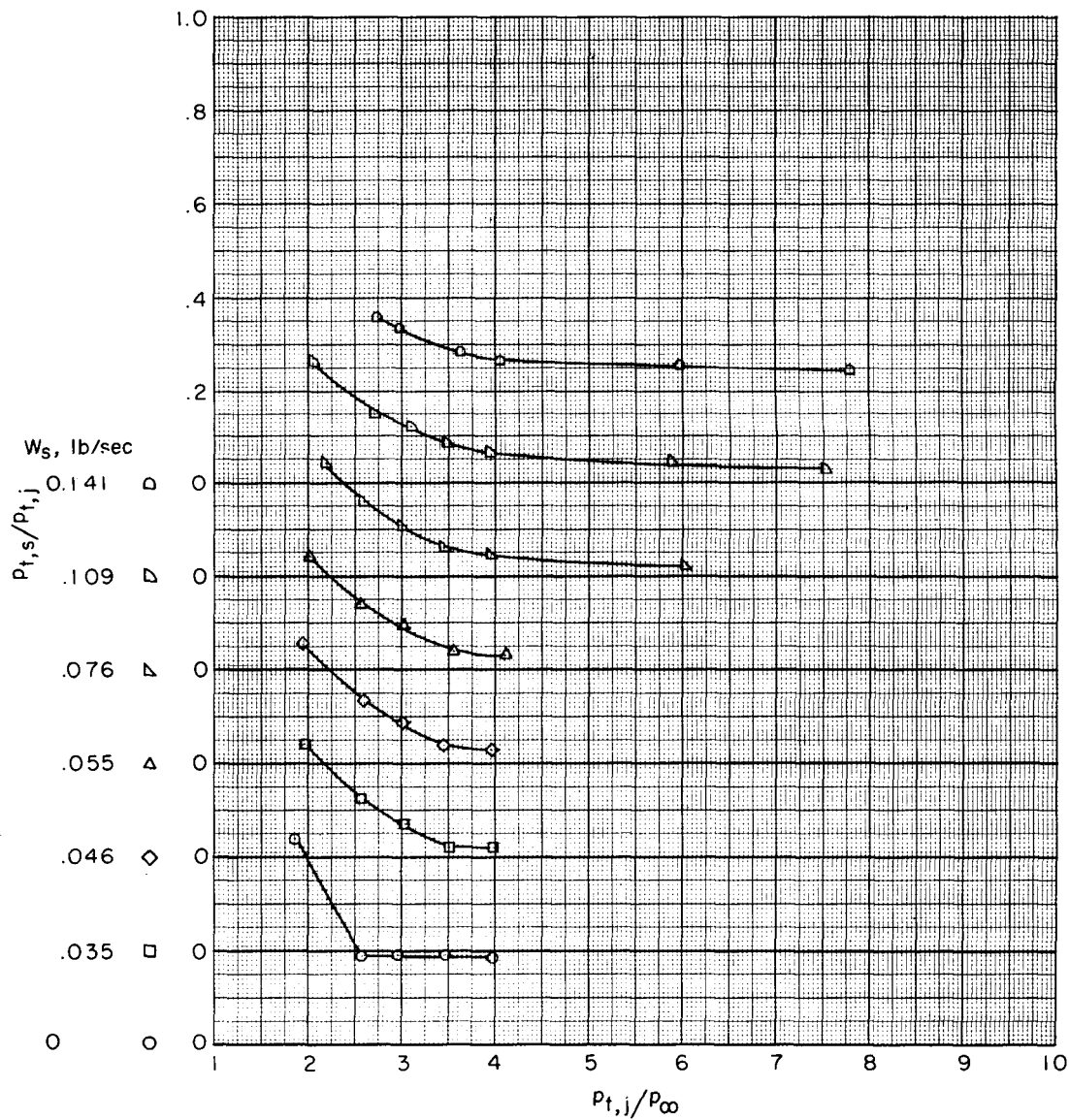
(e)  $M = 0.90$ ; afterburning nozzle.

Figure 6.- Continued.



(f)  $M = 0.95$ ; afterburning nozzle.

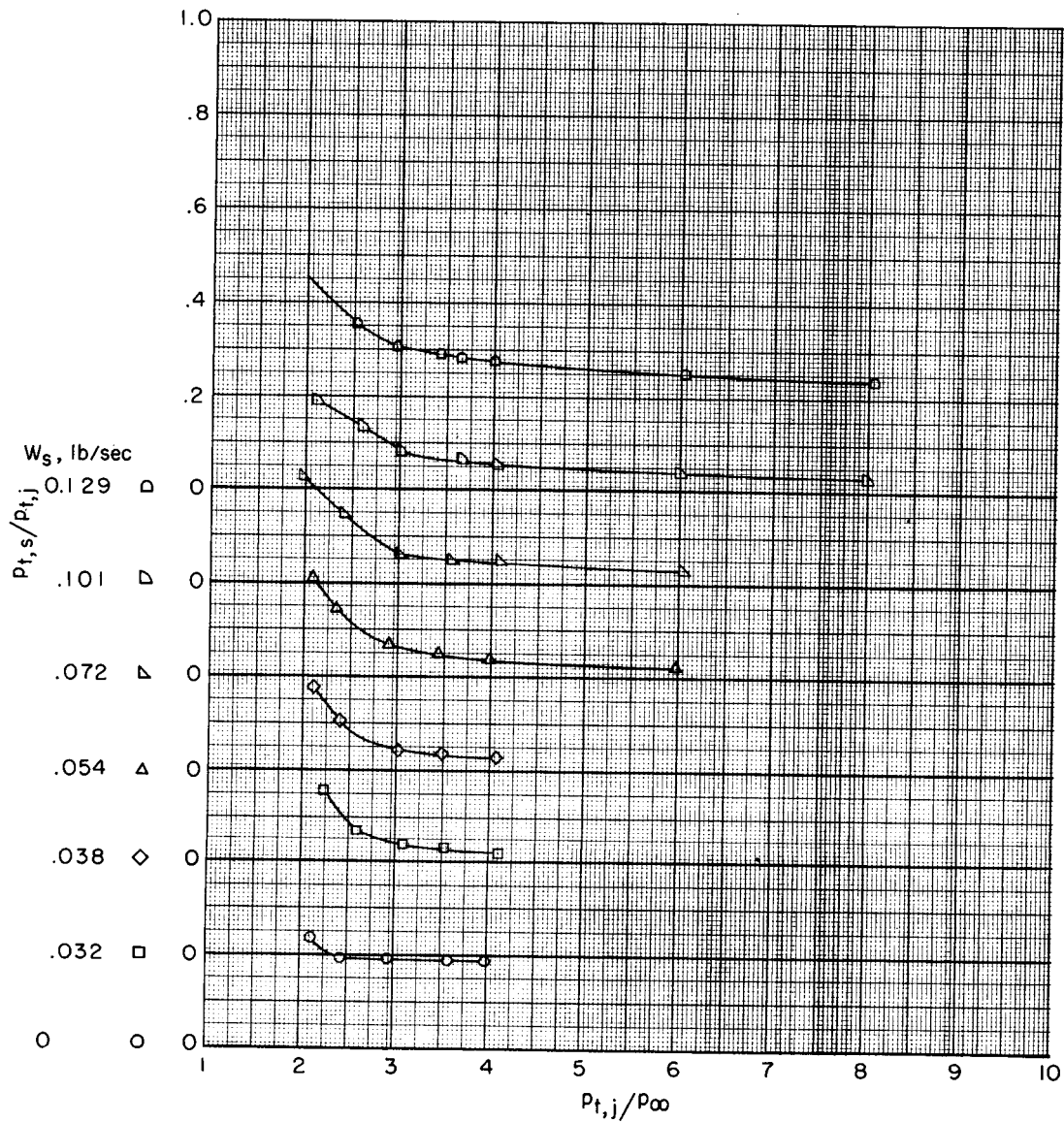
Figure 6.- Continued.



(g)  $M = 1.00$ ; afterburning nozzle.

Figure 6.- Continued.

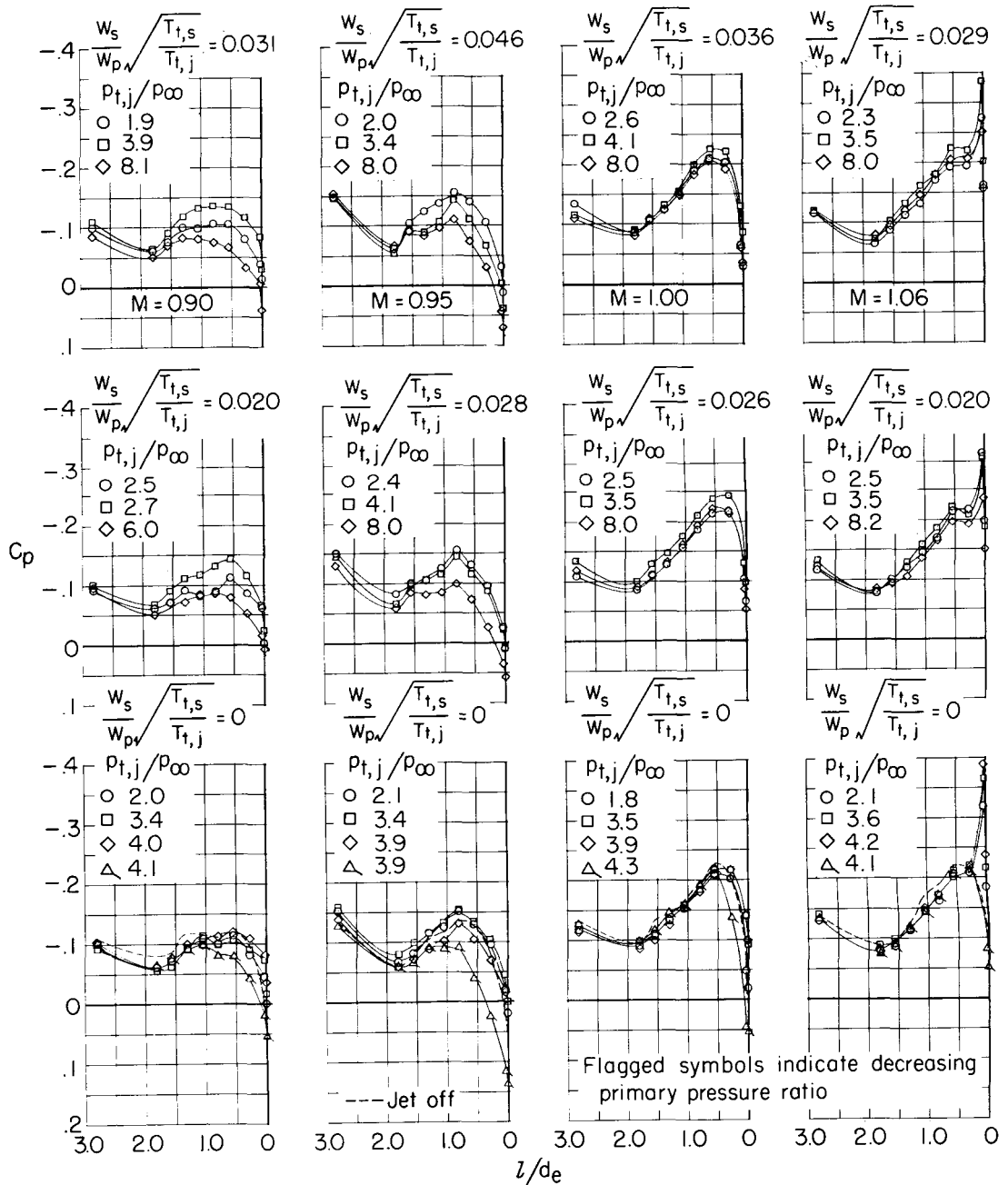




(h)  $M = 1.06$ ; afterburning nozzle.

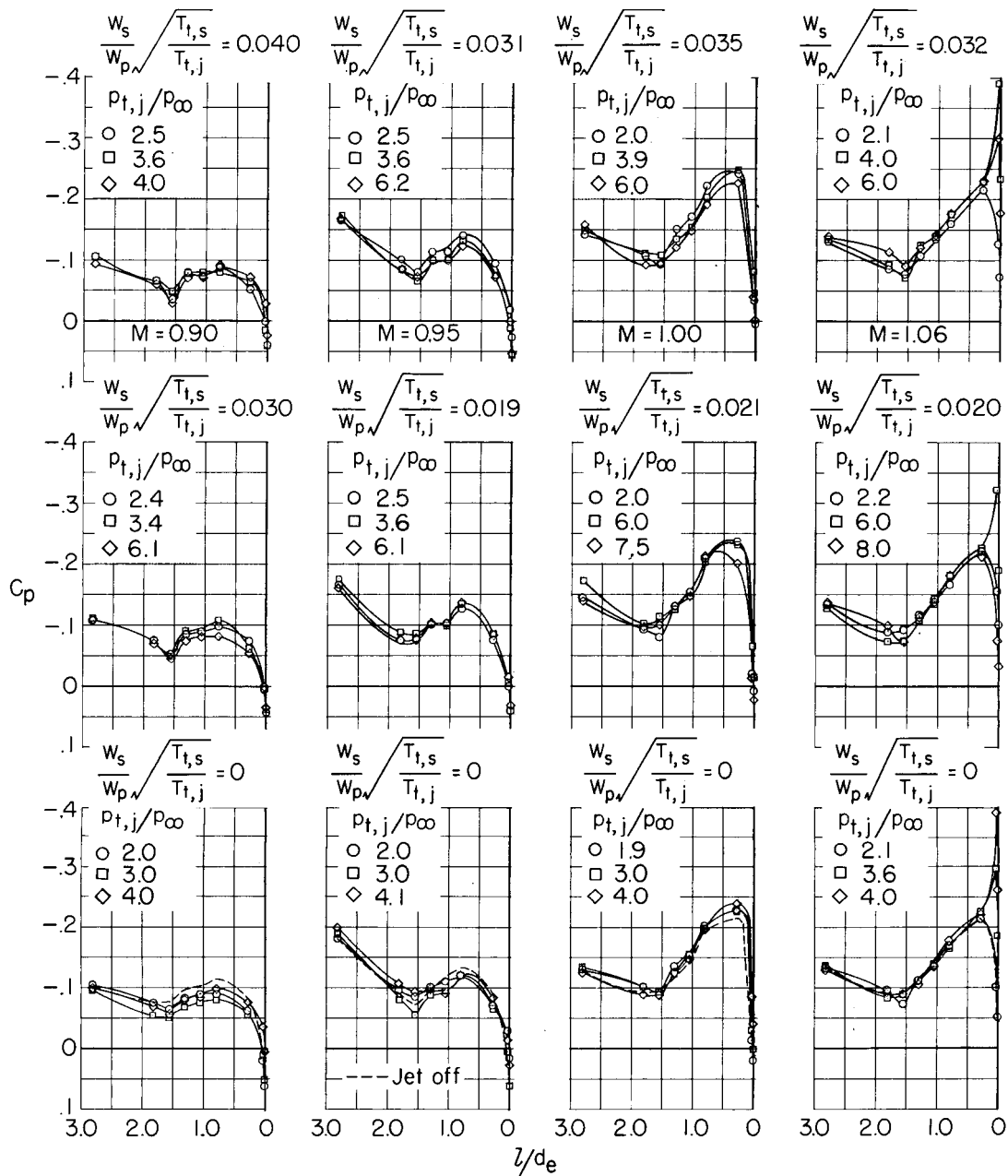
Figure 6.- Concluded.





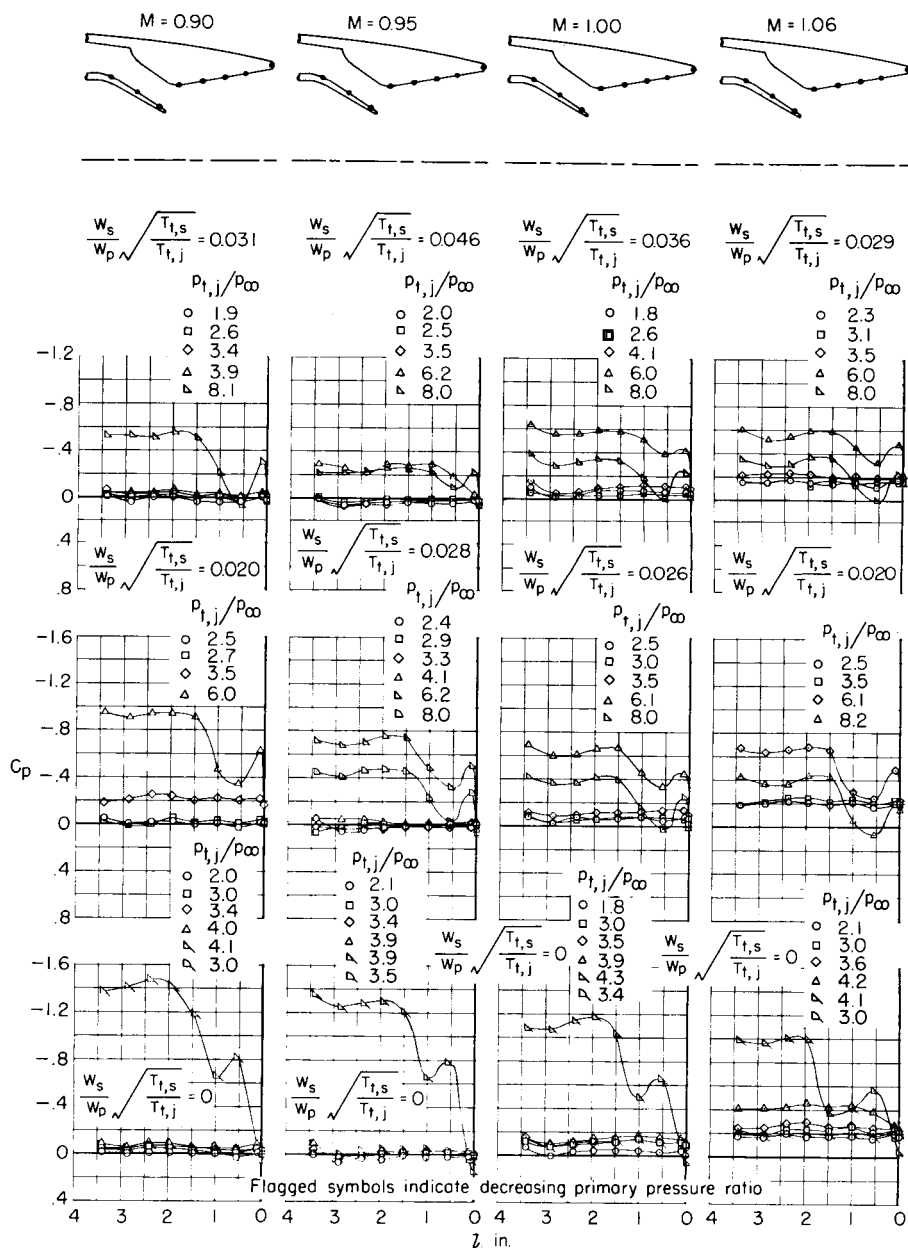
(a) Nonafterburning nozzle.

Figure 7.- Variation of afterbody pressure distributions with primary pressure ratios at several values of corrected weight-flow ratio. Row located at  $\theta = 0^\circ$ .



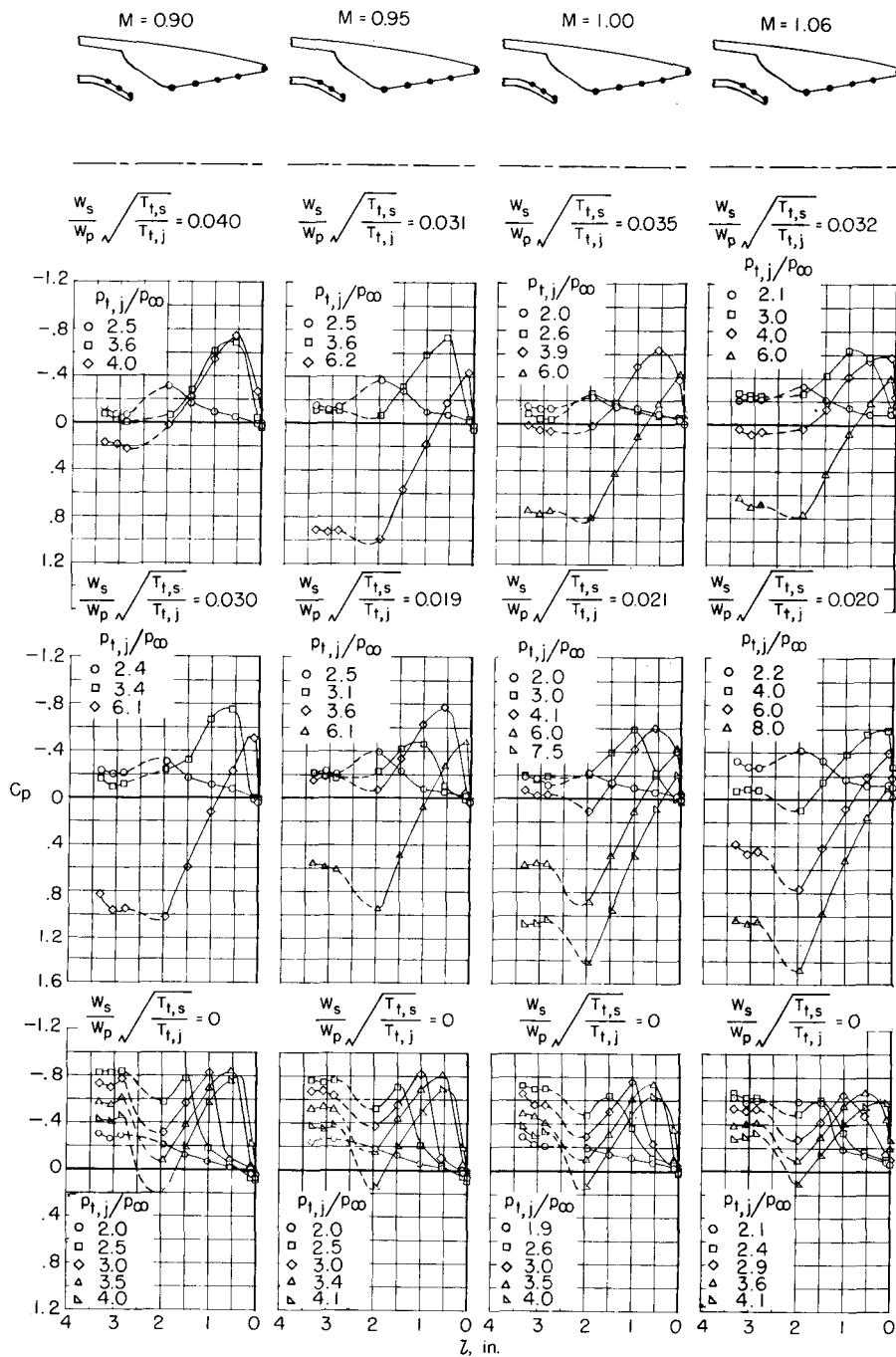
(b) Afterburning nozzle.

Figure 7.- Concluded.



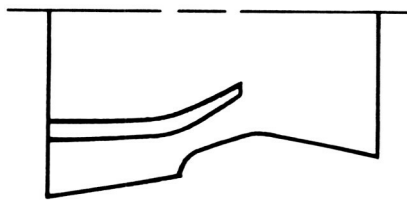
(a) Nonafterburning nozzle.

Figure 8.- Variation of pressure distributions over divergent ejector with primary pressure ratio for several values of corrected weight-flow ratio. Row located at  $\theta = 10^\circ$ .



(b) Afterburning nozzle.

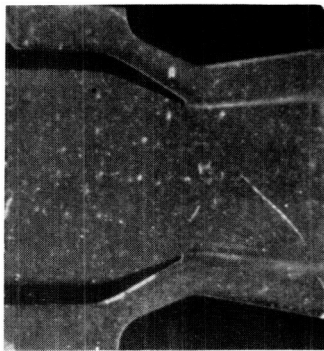
Figure 8.- Concluded.



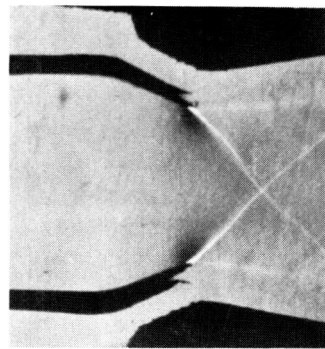
Sharp exit lip



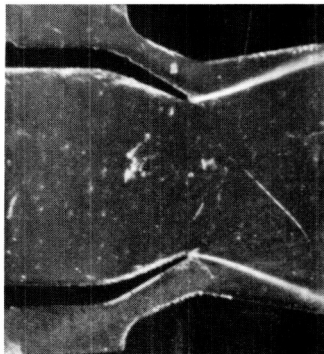
Flat exit lip



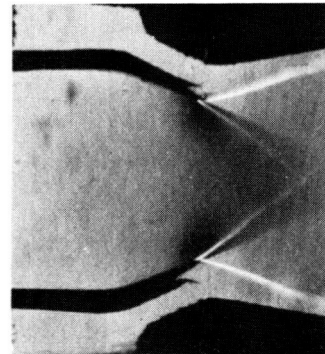
$$p_{t,j}/p_{\infty} = 3.1$$



$$p_{t,j}/p_{\infty} = 3.1$$



$$p_{t,j}/p_{\infty} = 5.0$$



$$p_{t,j}/p_{\infty} = 5.0$$

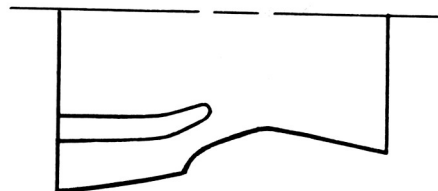
(a) Nonafterburning nozzle.

L-58-1a.1

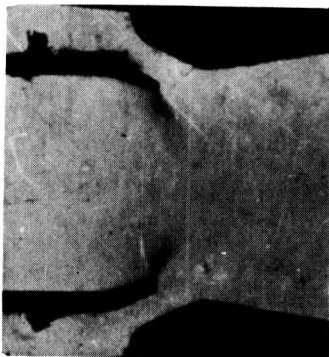
Figure 9.- Effect of primary nozzle exit shape on the primary jet boundary.  $M = 0$ ;  $W_s = 0$ .



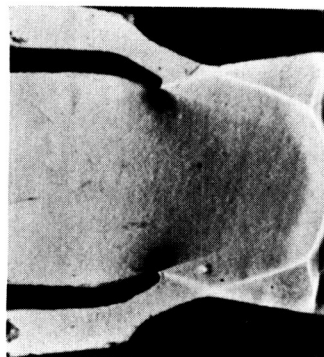
Sharp exit lip



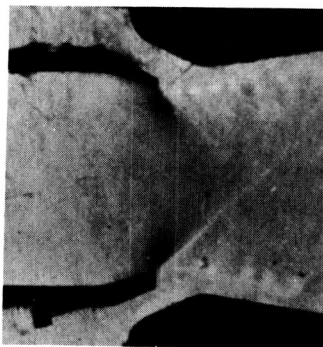
Rounded exit lip



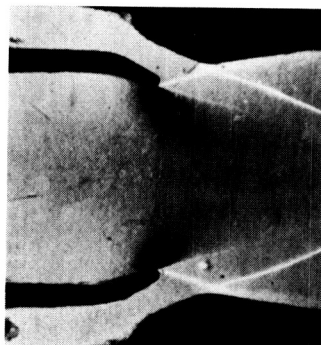
$p_{t,j}/p_{\infty} = 3.1$



$p_{t,j}/p_{\infty} = 3.1$



$p_{t,j}/p_{\infty} = 5.0$



$p_{t,j}/p_{\infty} = 5.0$

(b) Afterburning nozzle.

L-58-2a.1

Figure 9.- Concluded.

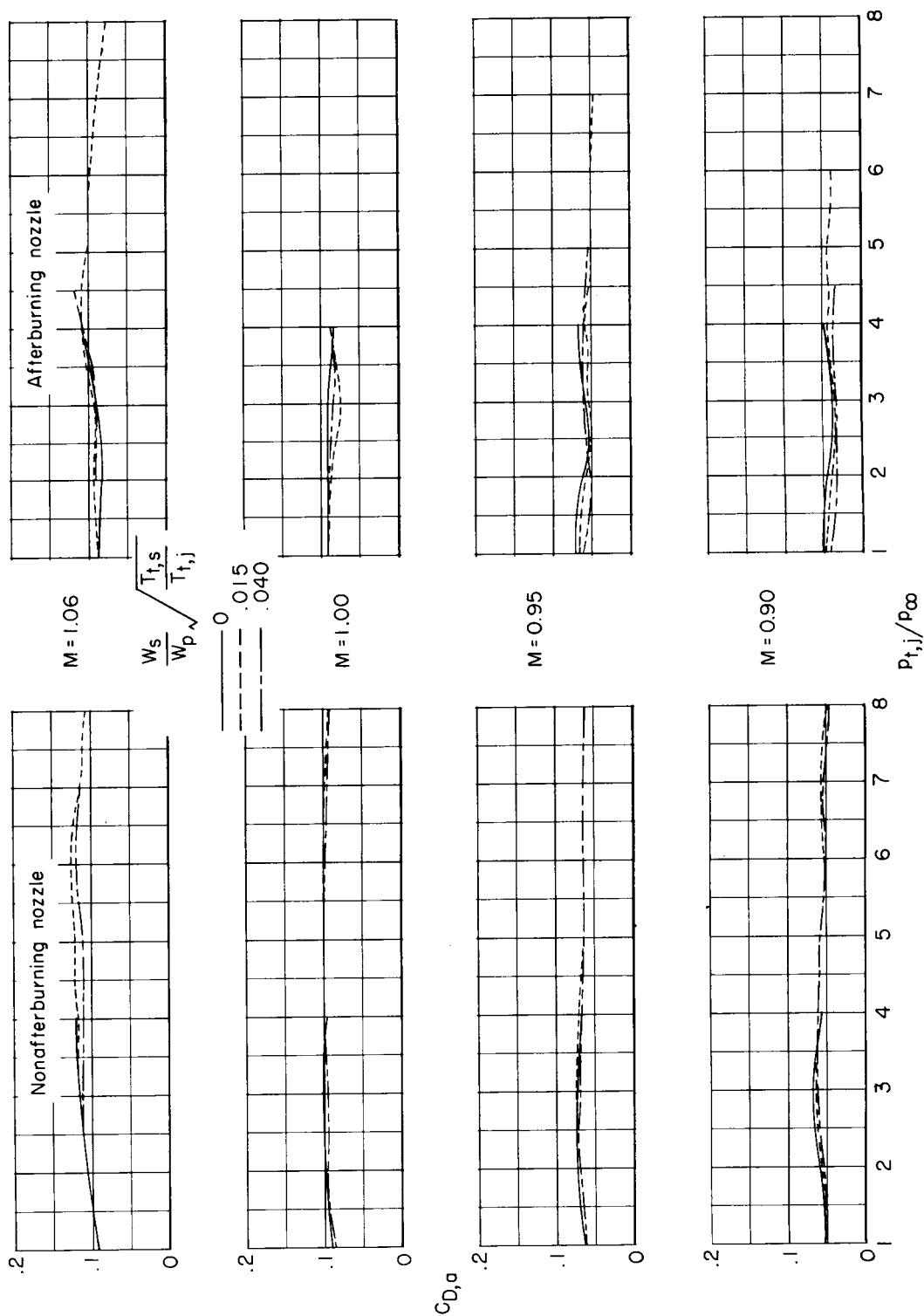


Figure 10.- Variation of afterbody pressure-drag coefficient with primary pressure ratio at several values of corrected weight-flow ratio.

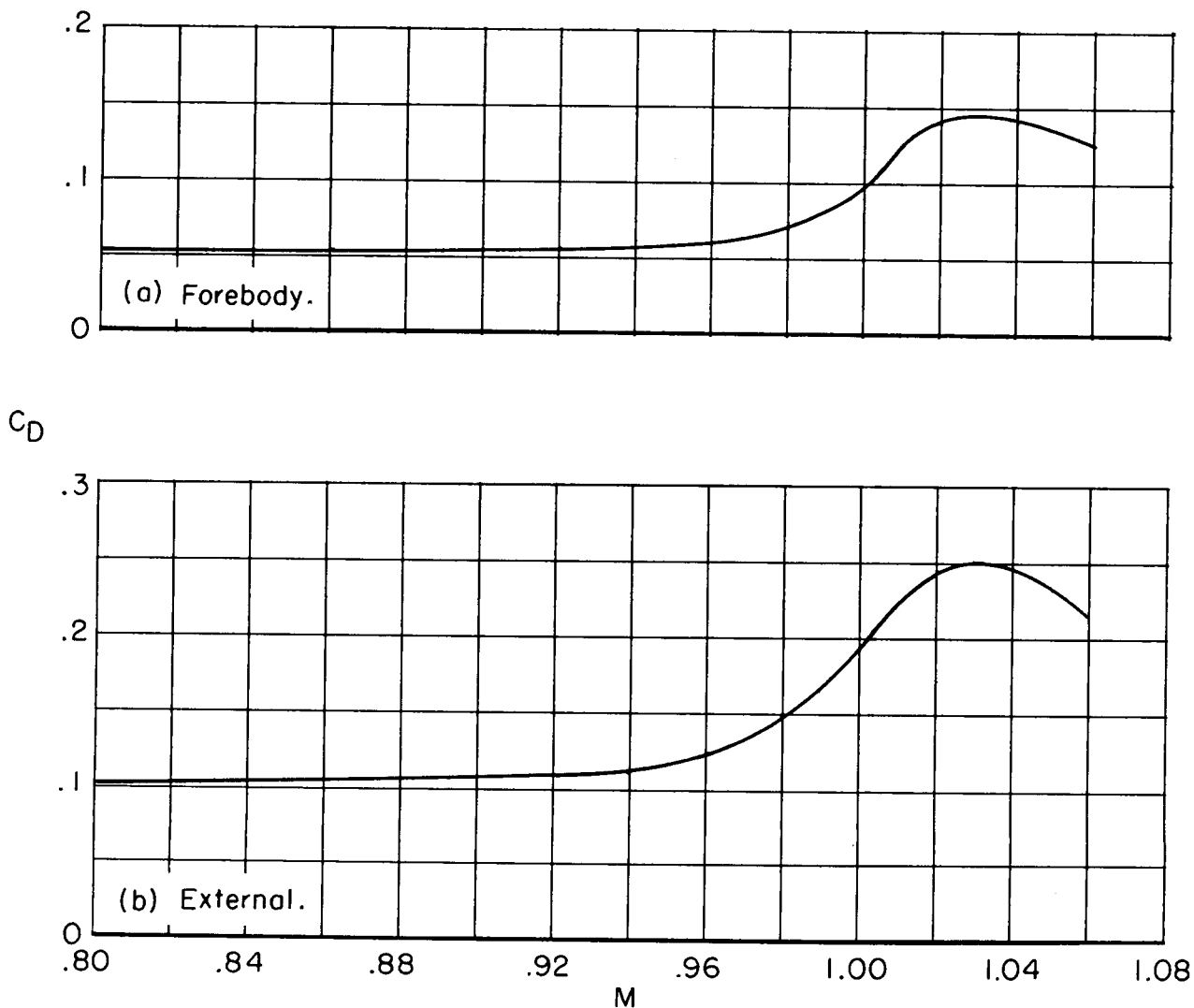
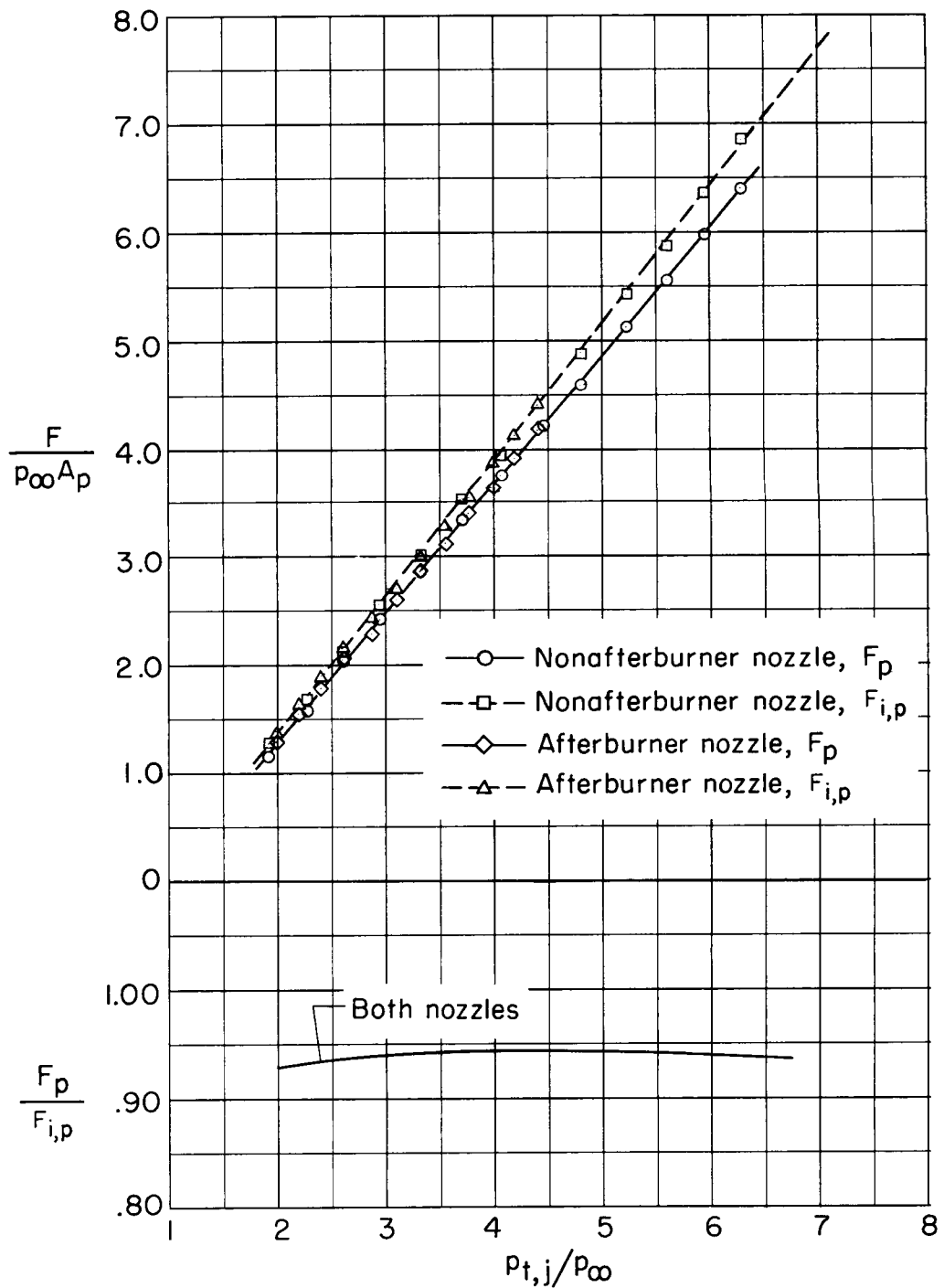


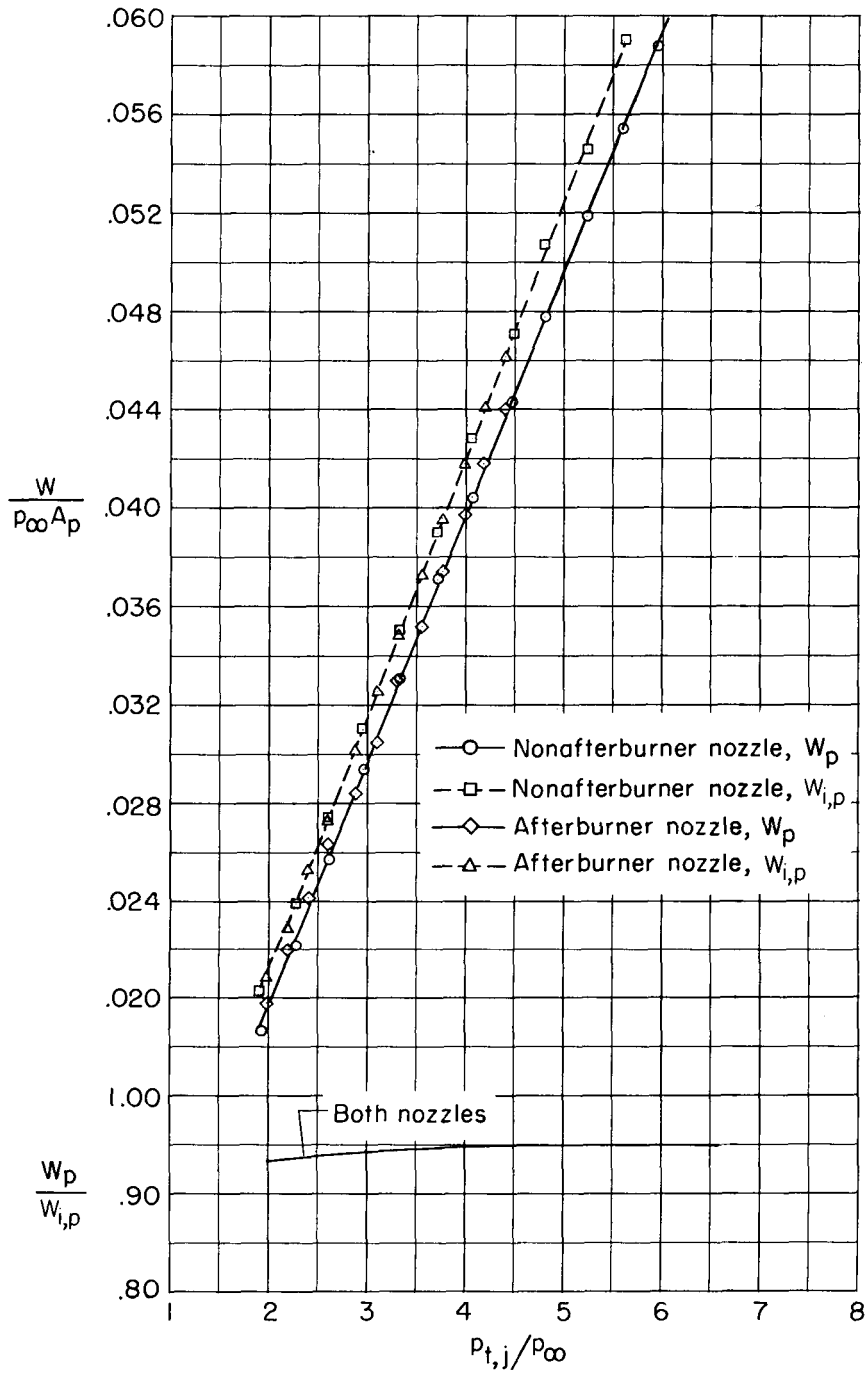
Figure 11.- Variation of jet-off model drag coefficient with Mach number.  
Secondary air off.





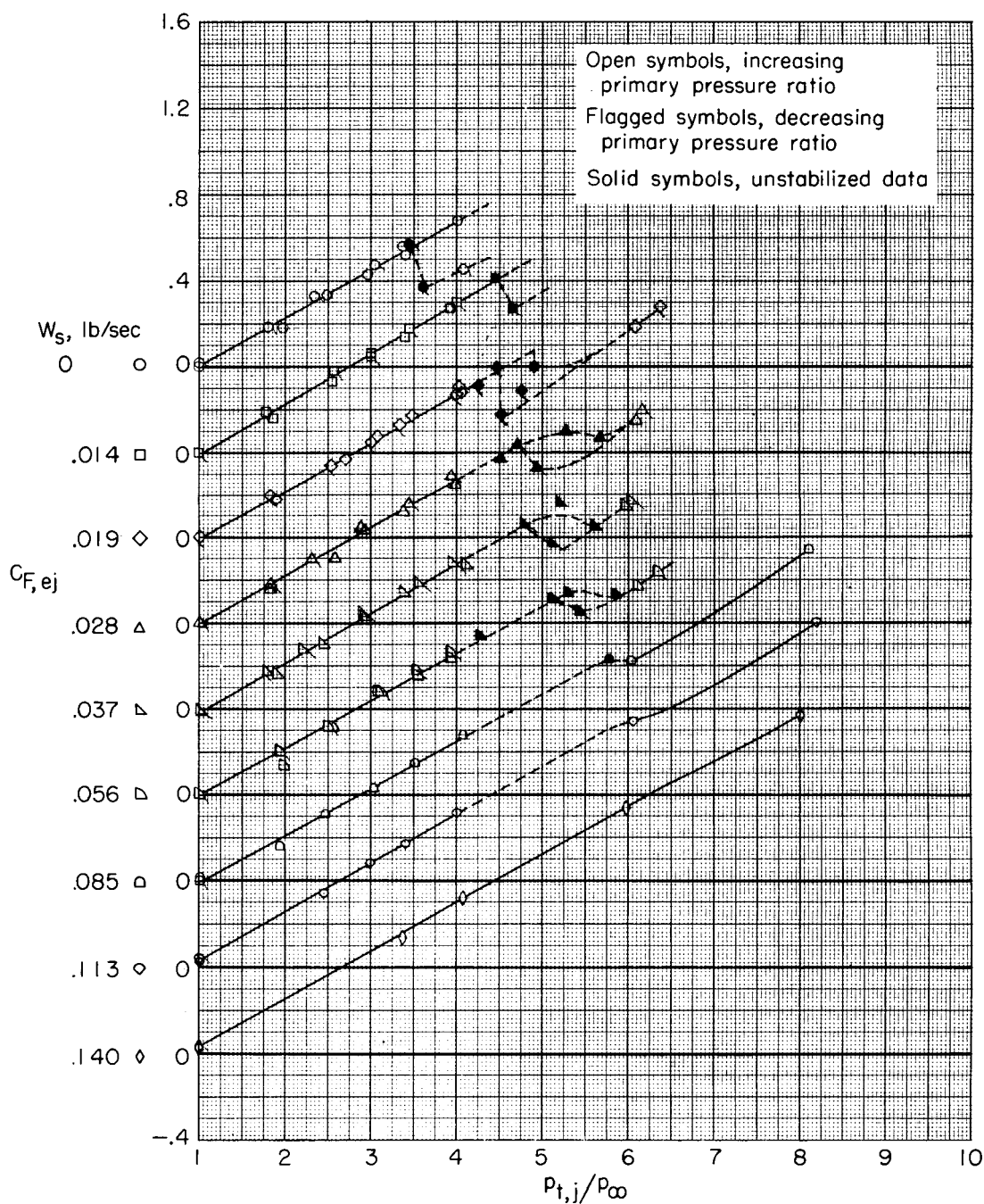
(a) Thrust characteristics.

Figure 12.- Performance of primary nozzles (no ejector shroud).  $M = 0$ .



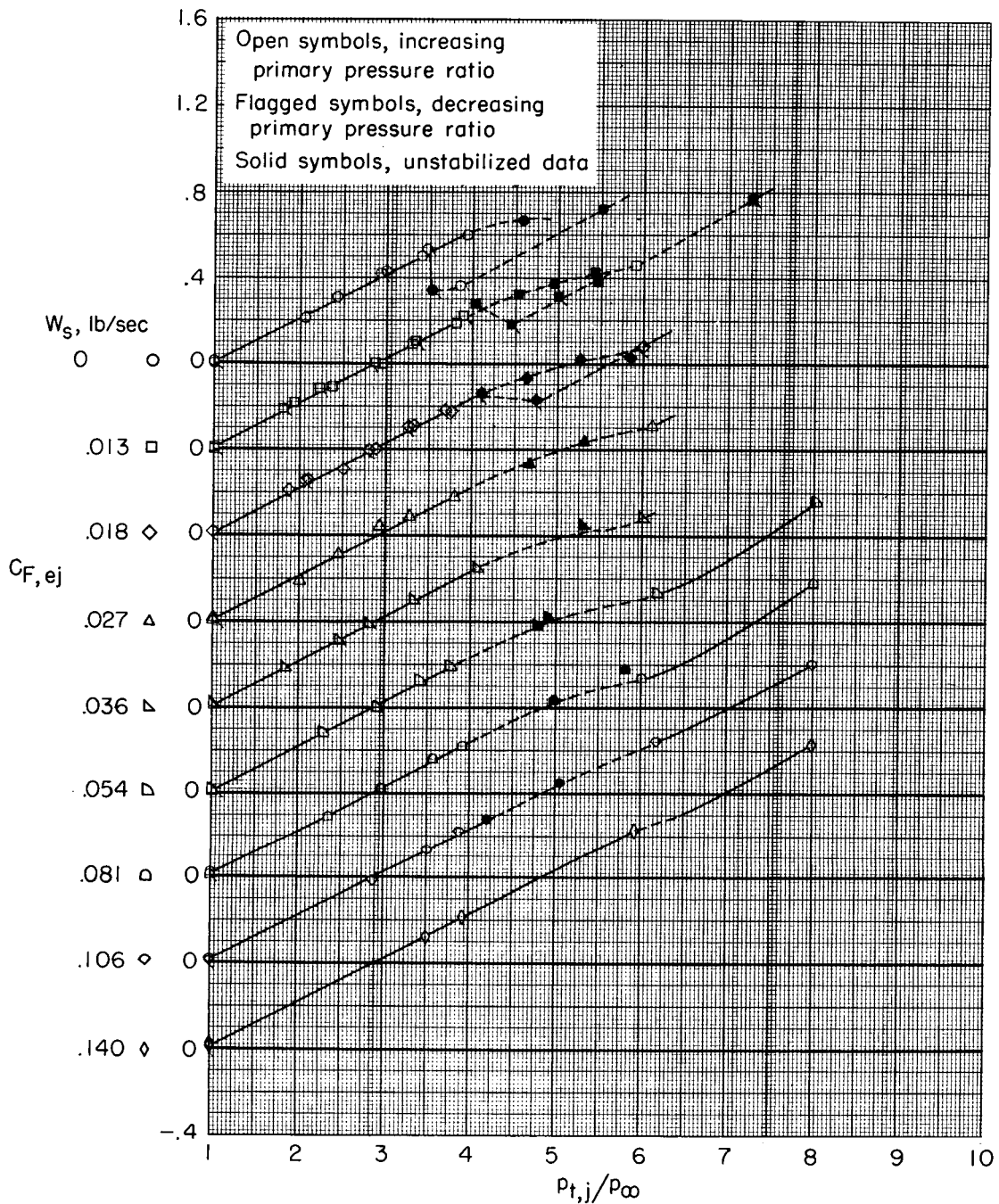
(b) Flow characteristics.

Figure 12.- Concluded.



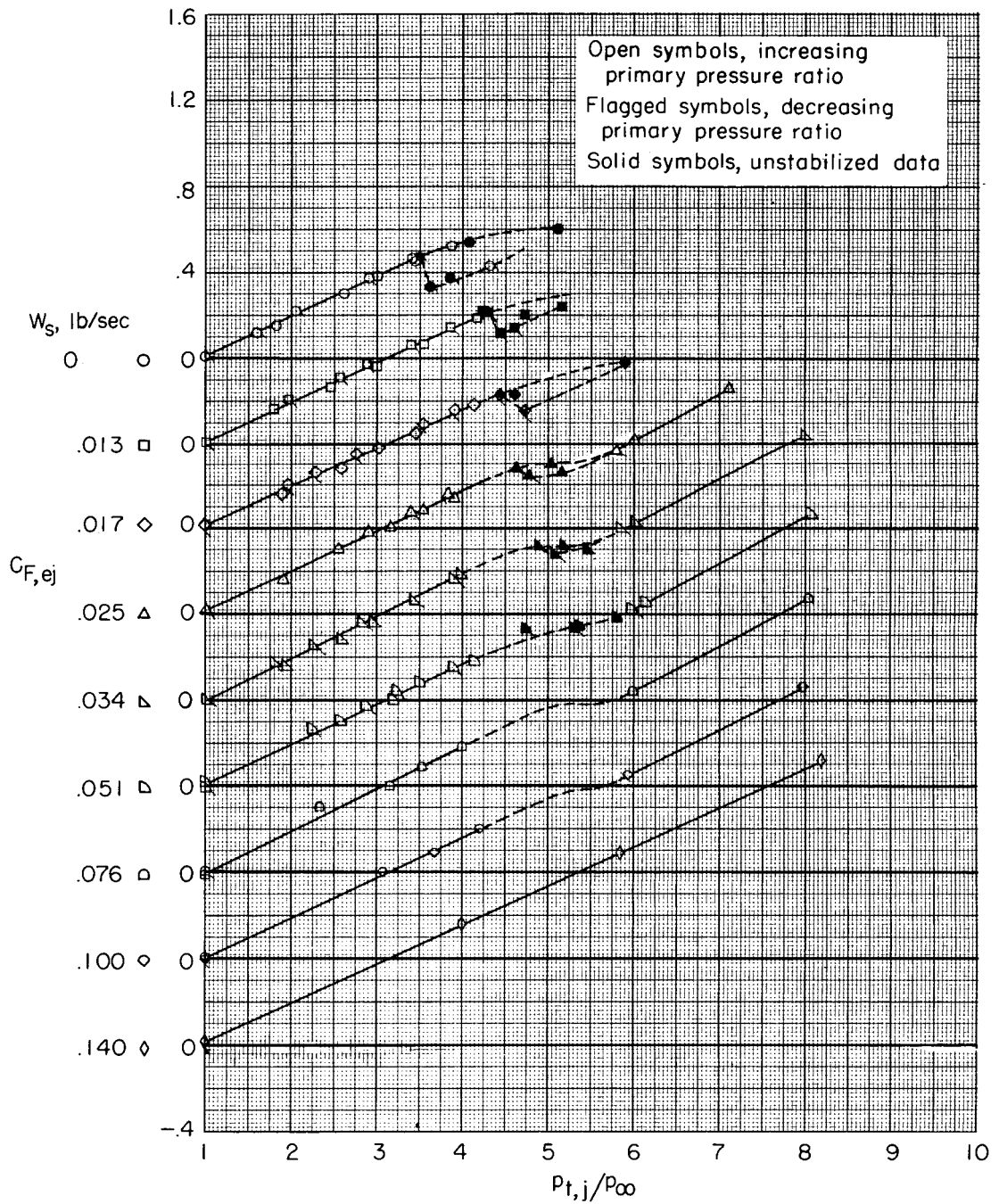
(a)  $M = 0.90$ ; nonafterburning nozzle.

Figure 13.- Variation of gross ejector thrust coefficient with primary pressure ratio at constant values of secondary air weight flow.



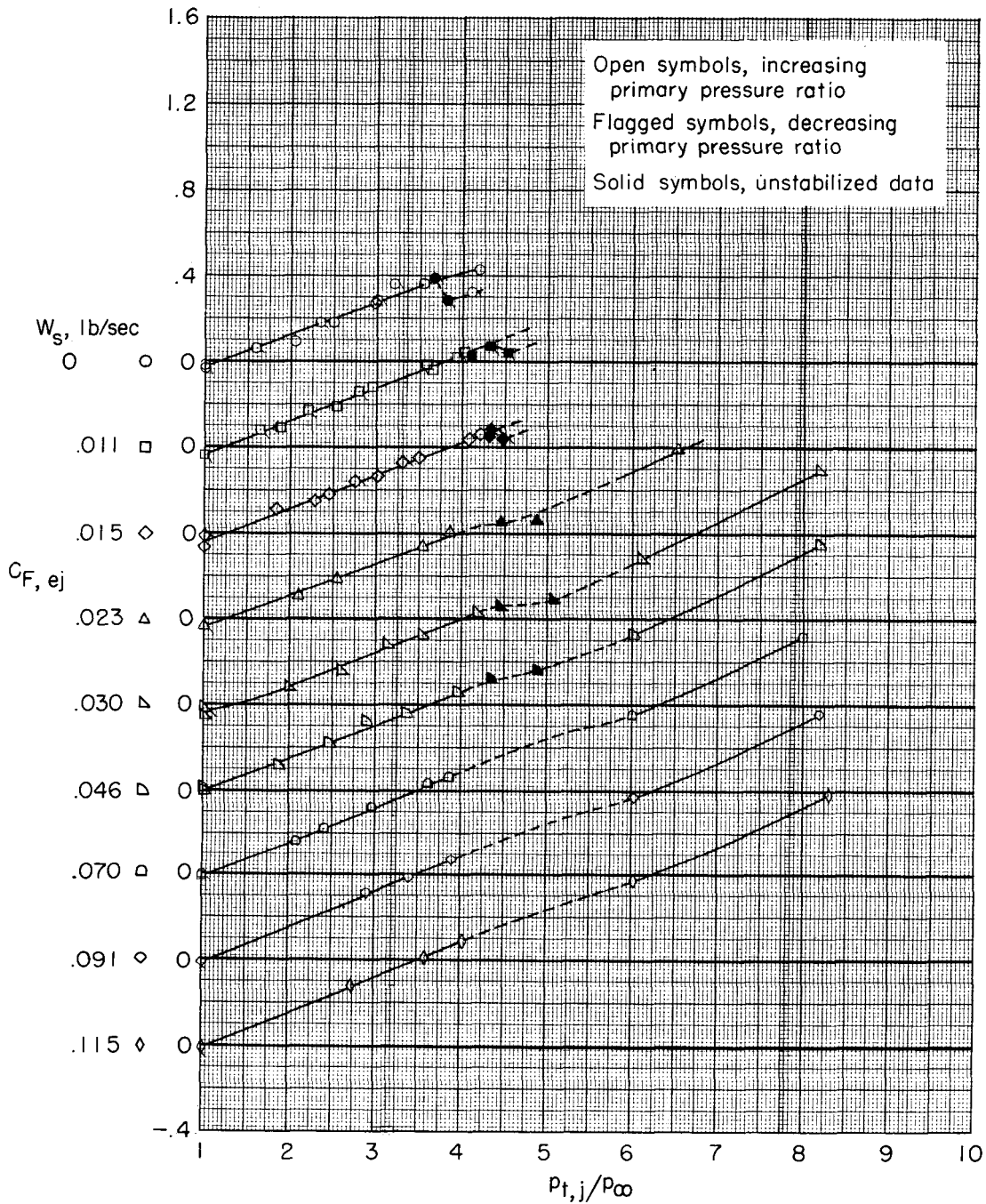
(b)  $M = 0.95$ ; nonafterburning nozzle.

Figure 13.- Continued.



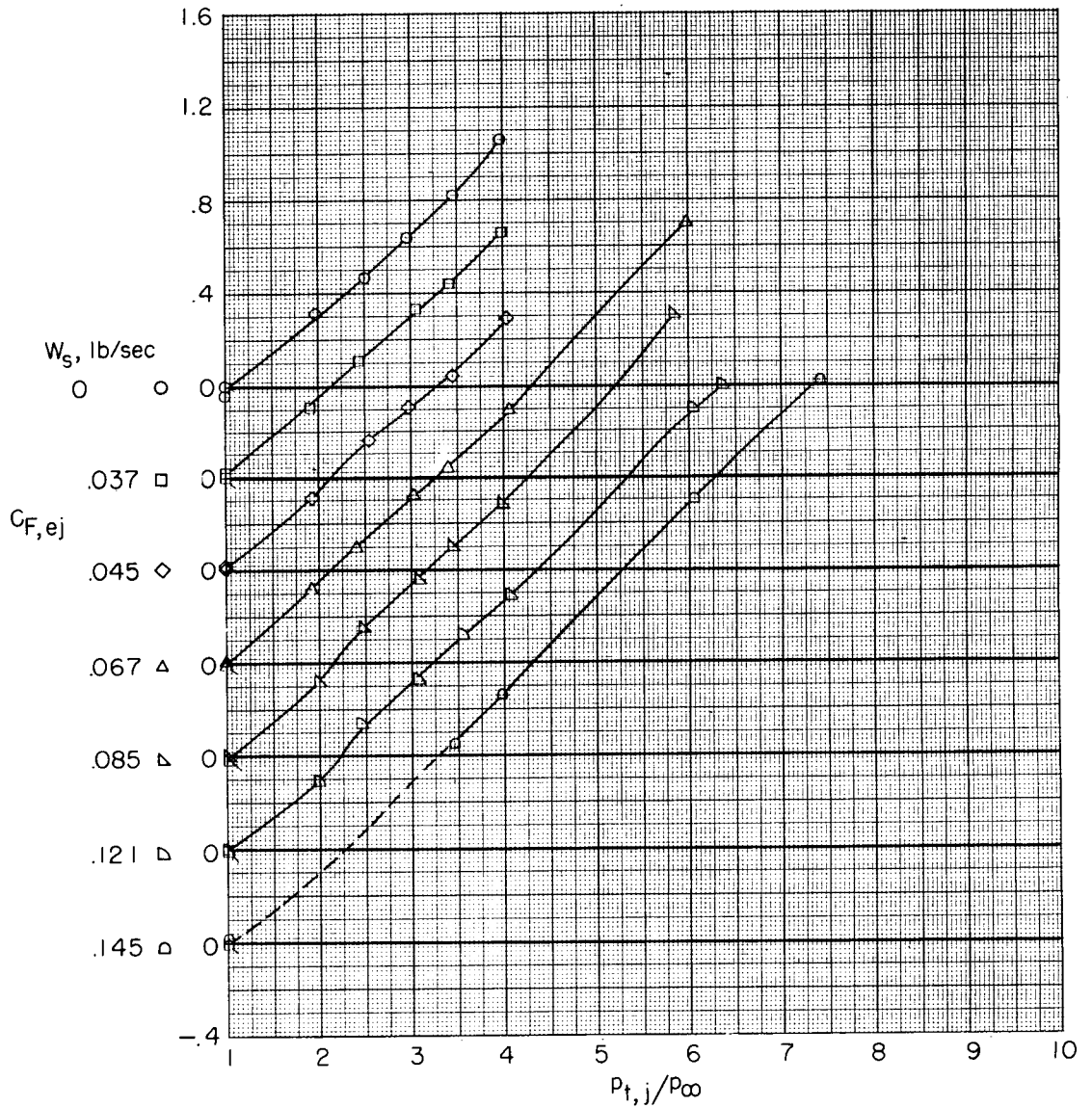
(c)  $M = 1.00$ ; nonafterburning nozzle.

Figure 13.- Continued.



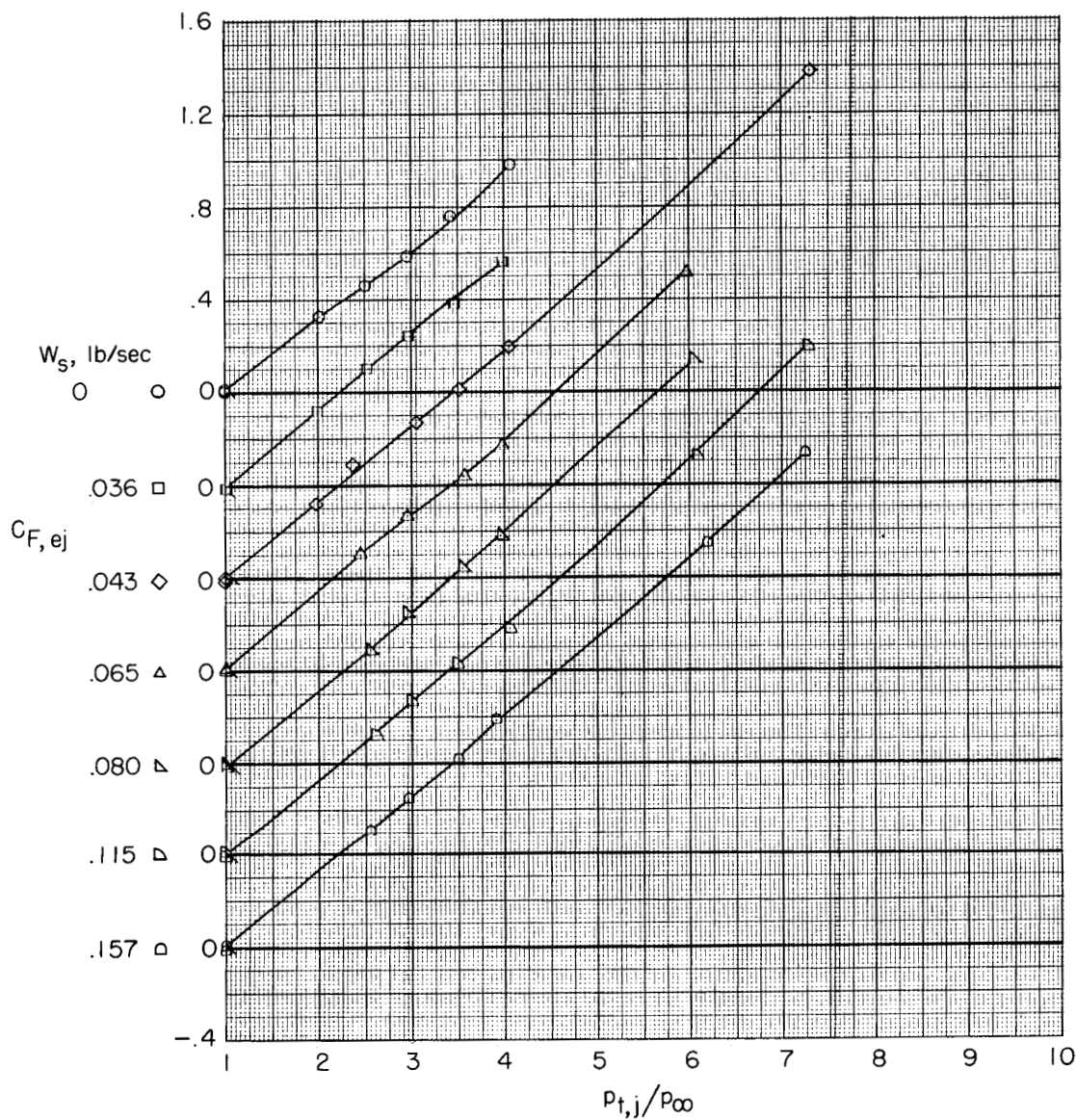
(d)  $M = 1.06$ ; nonafterburning nozzle.

Figure 13.- Continued.



(e)  $M = 0.90$ ; afterburning nozzle.

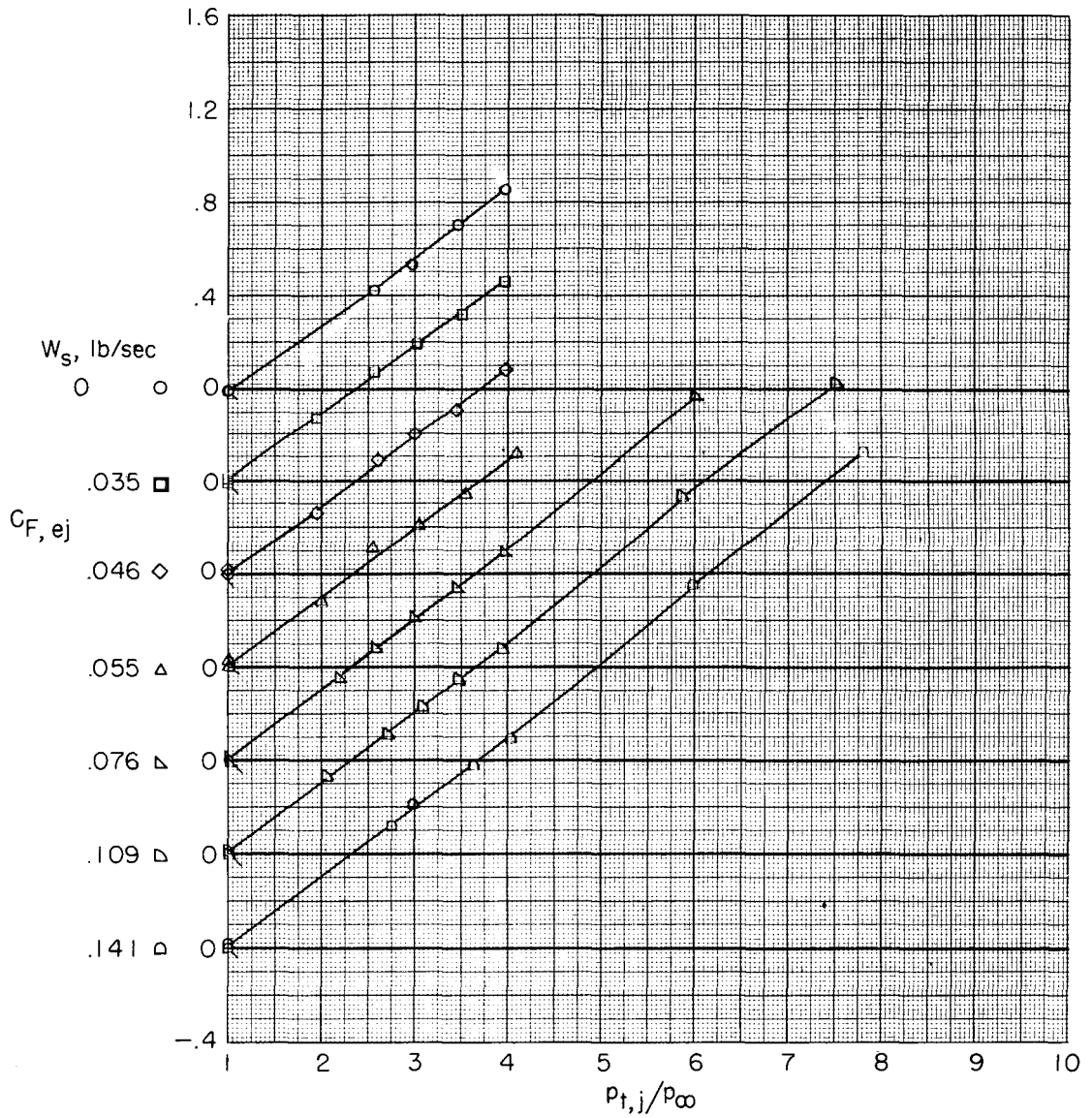
Figure 13.- Continued.



(f)  $M = 0.95$ ; afterburning nozzle.

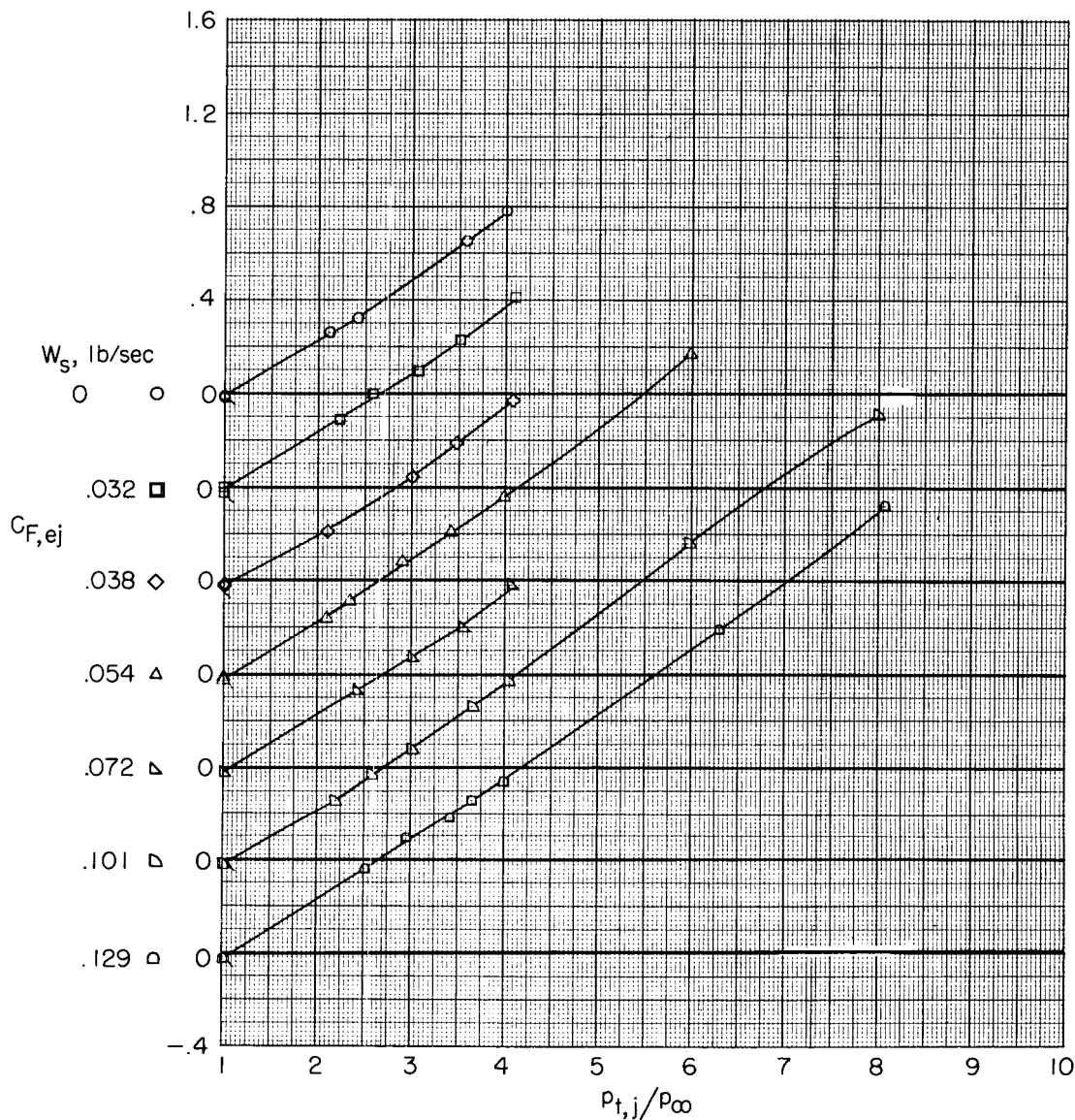
Figure 13.- Continued.





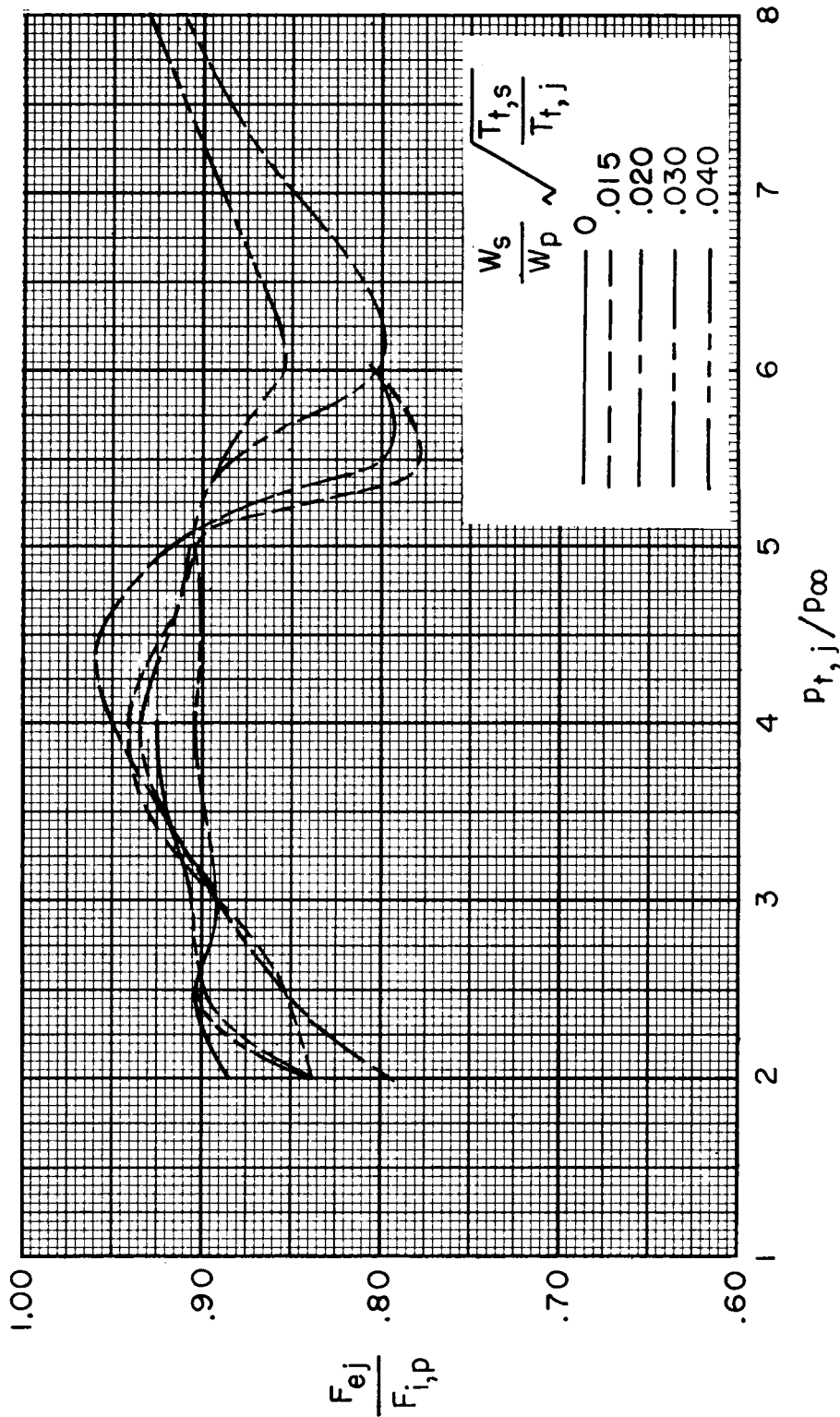
(g)  $M = 1.00$ ; afterburning nozzle.

Figure 13.- Continued.



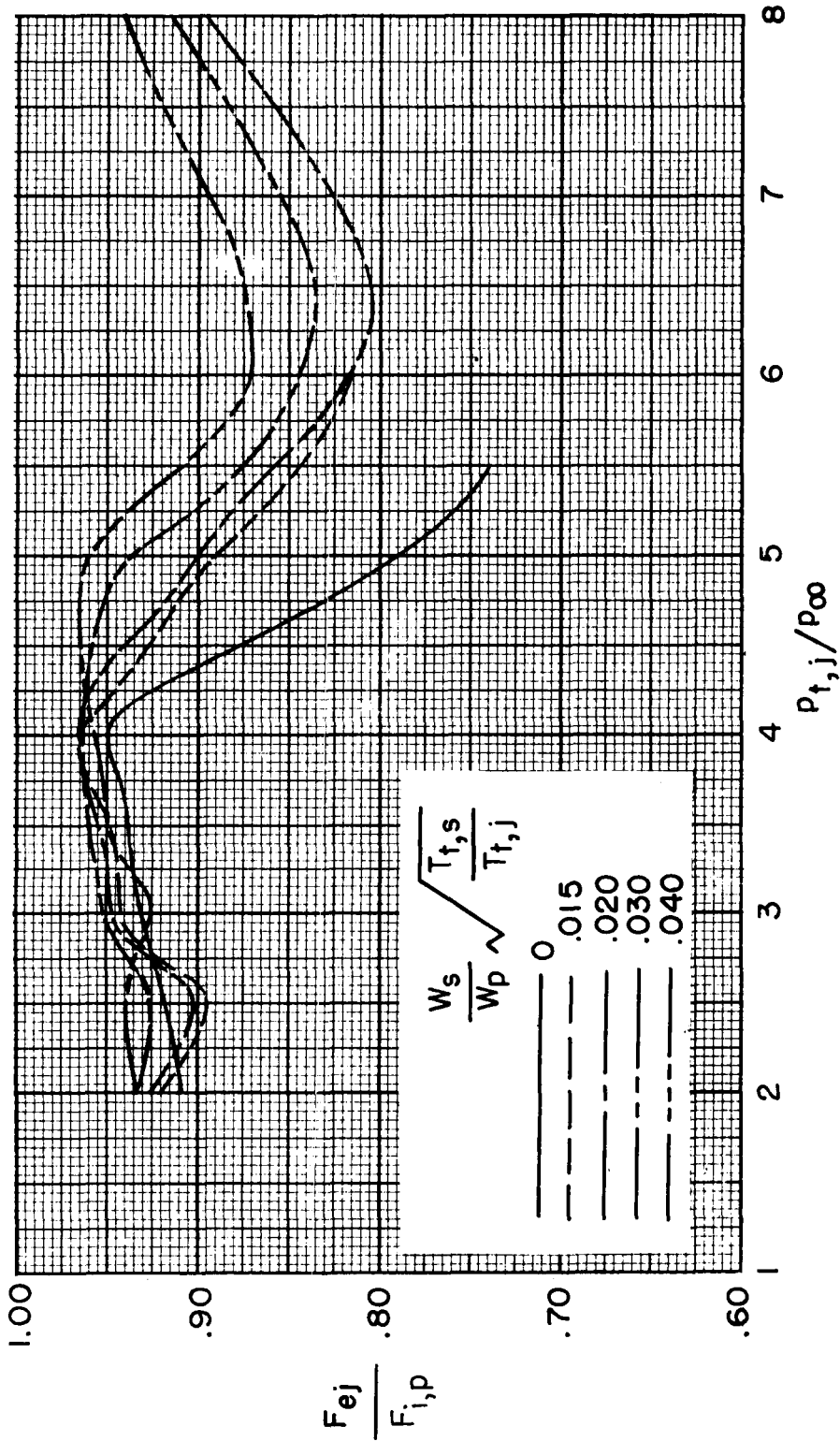
(h)  $M = 1.06$ ; afterburning nozzle.

Figure 13.- Concluded.



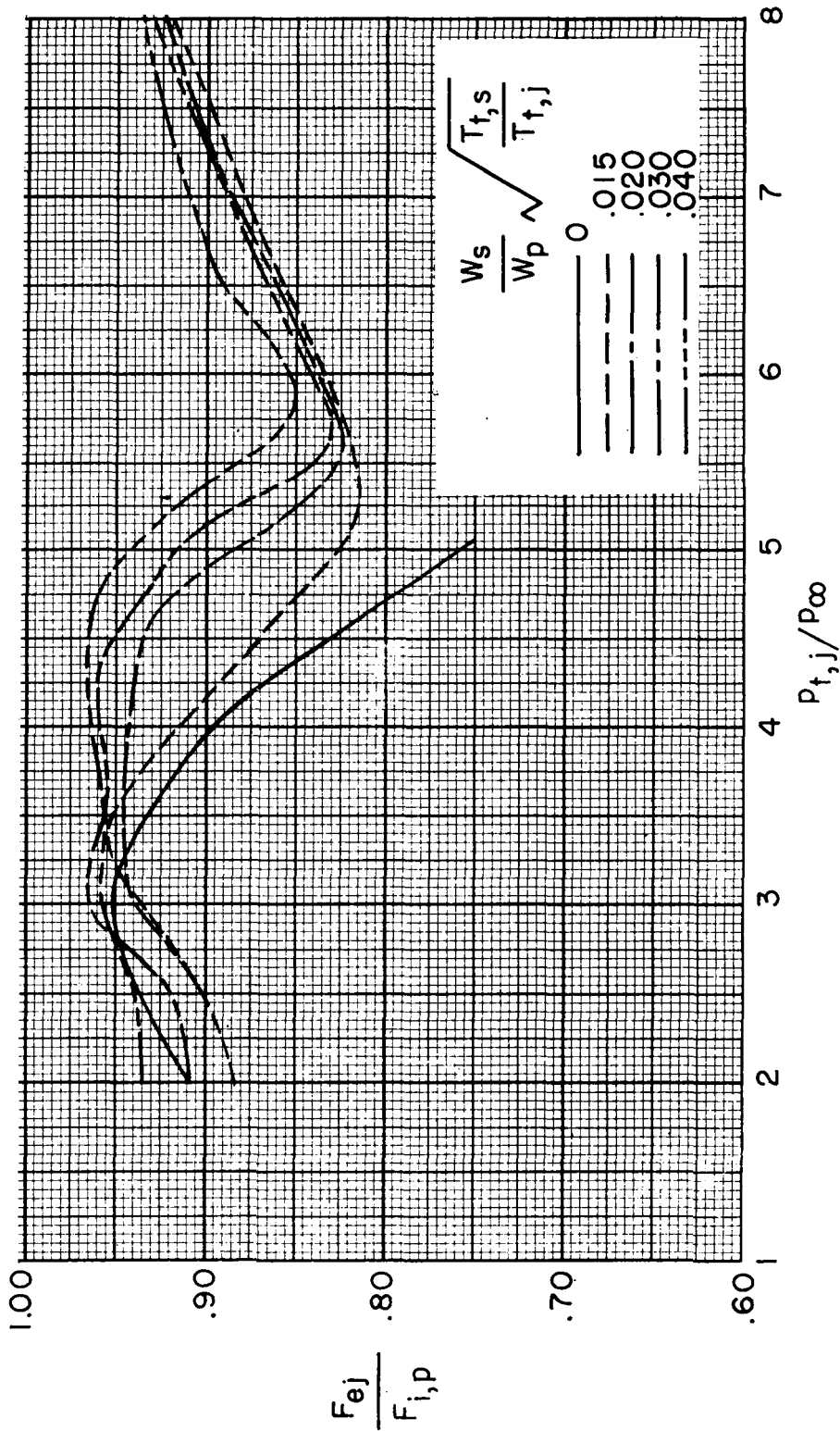
(a)  $M = 0.90$ ; nonafterburning nozzle.

Figure 14.- Variation of ejector thrust ratio with primary pressure ratio at constant values of corrected weight-flow ratio.



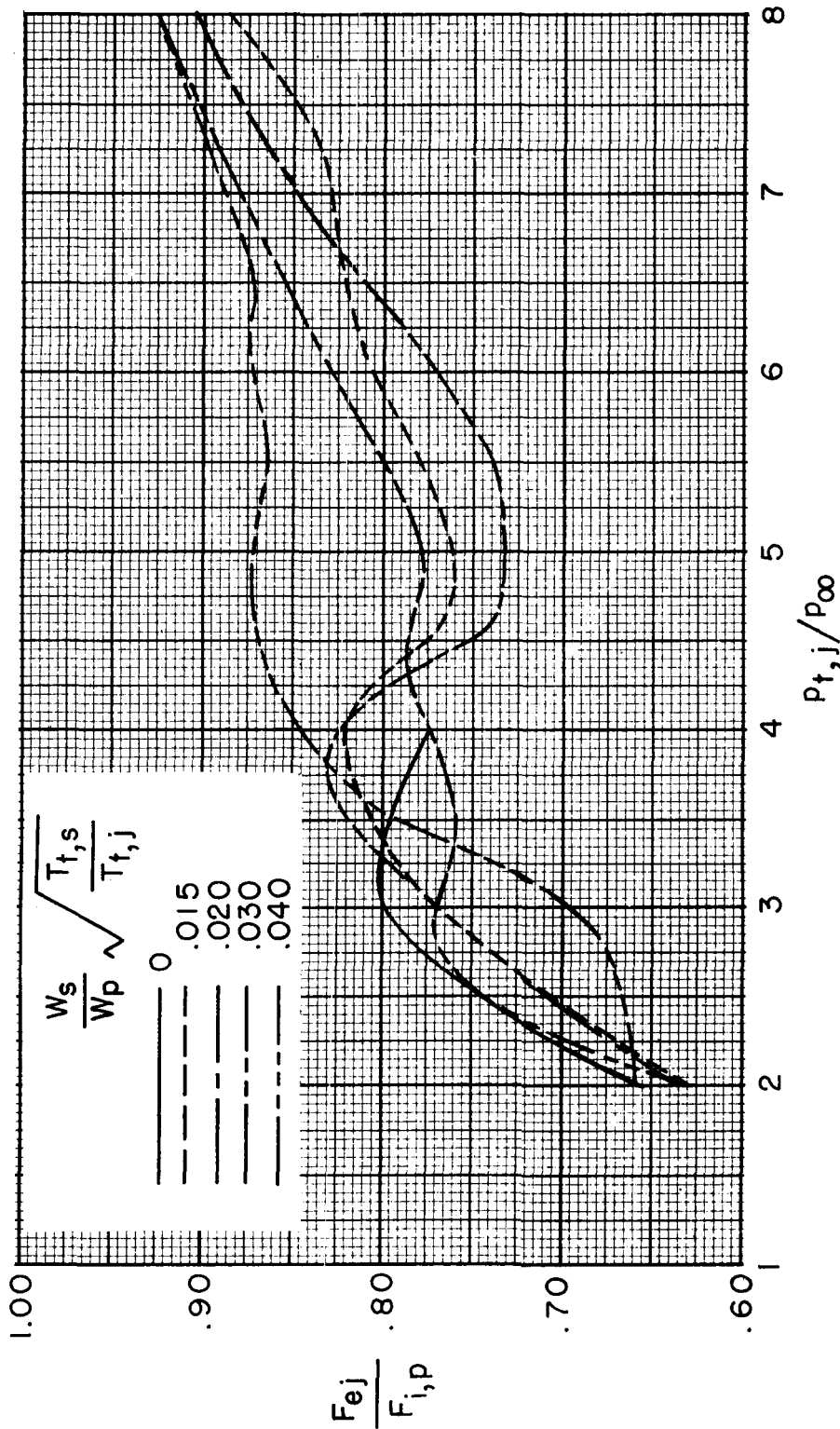
(b)  $M = 0.95$ ; nonafterburning nozzle.

Figure 14.- Continued.



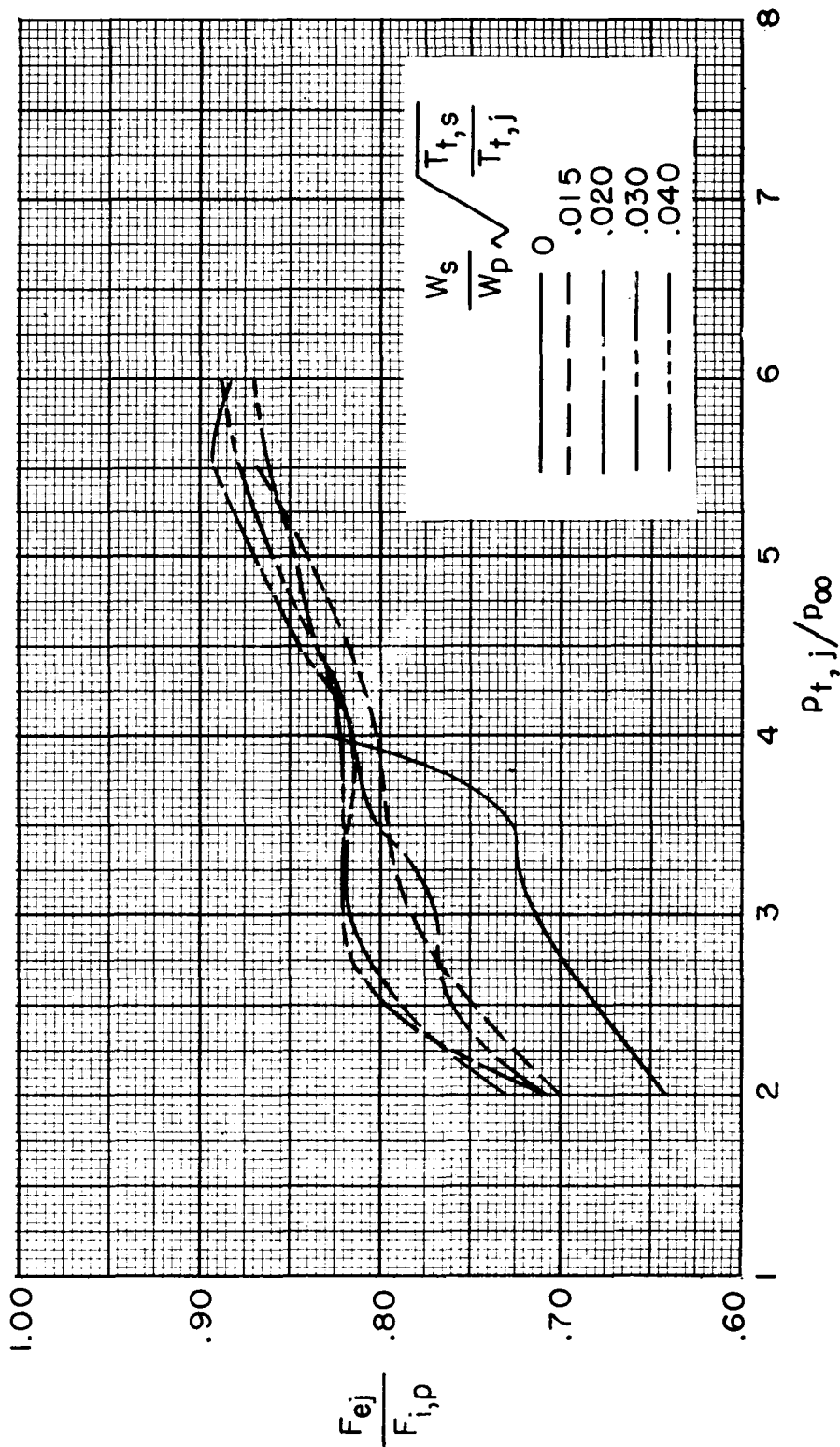
(c)  $M = 1.00$ ; nonafterburning nozzle.

Figure 14.- Continued.



(d)  $M = 1.06$ ; nonafterburning nozzle.

Figure 14.- Continued.



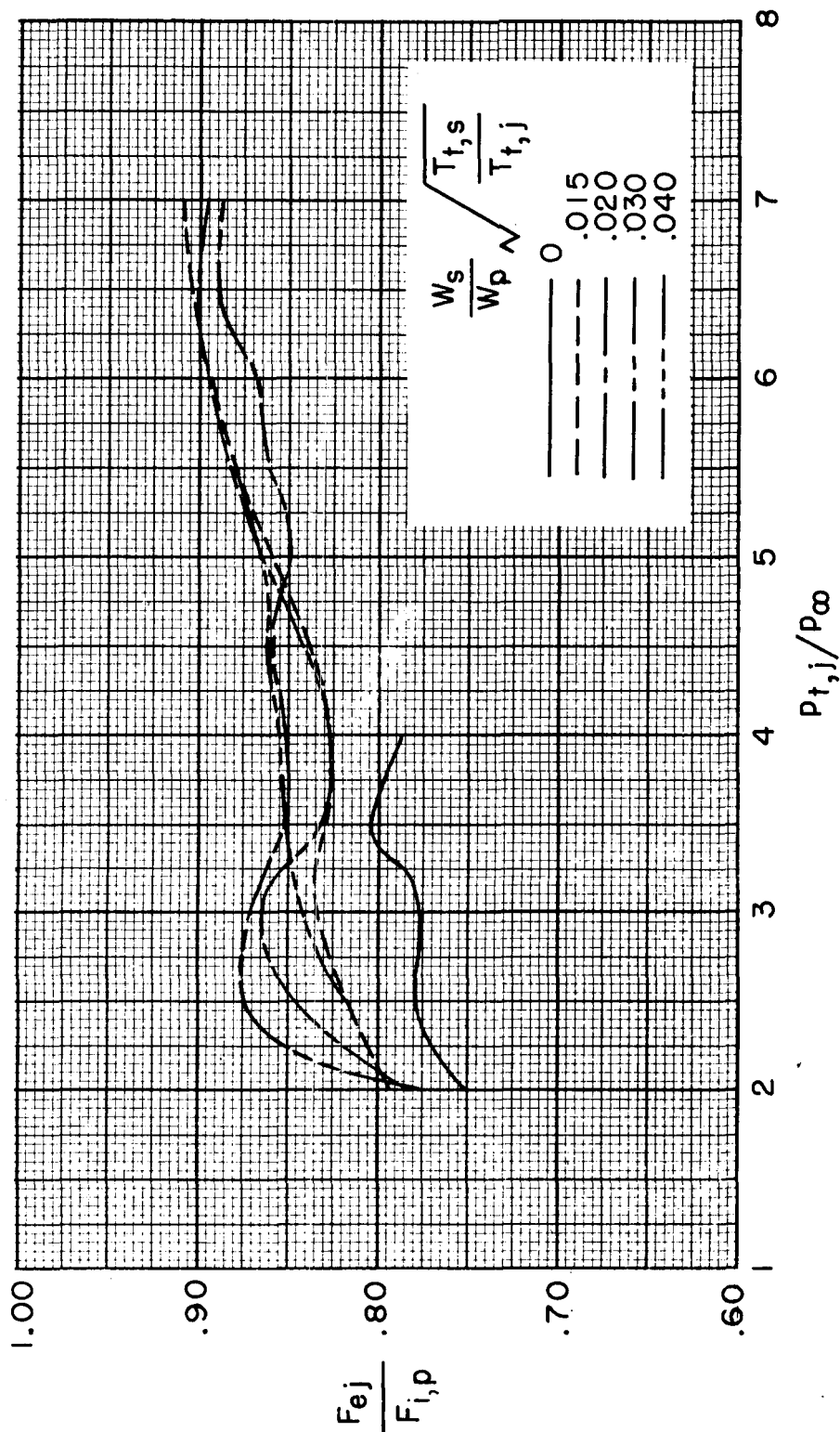
(e)  $M = 0.90$ ; afterburning nozzle.

Figure 14.- Continued.

UNCLASSIFIED

CONFIDENTIAL

59

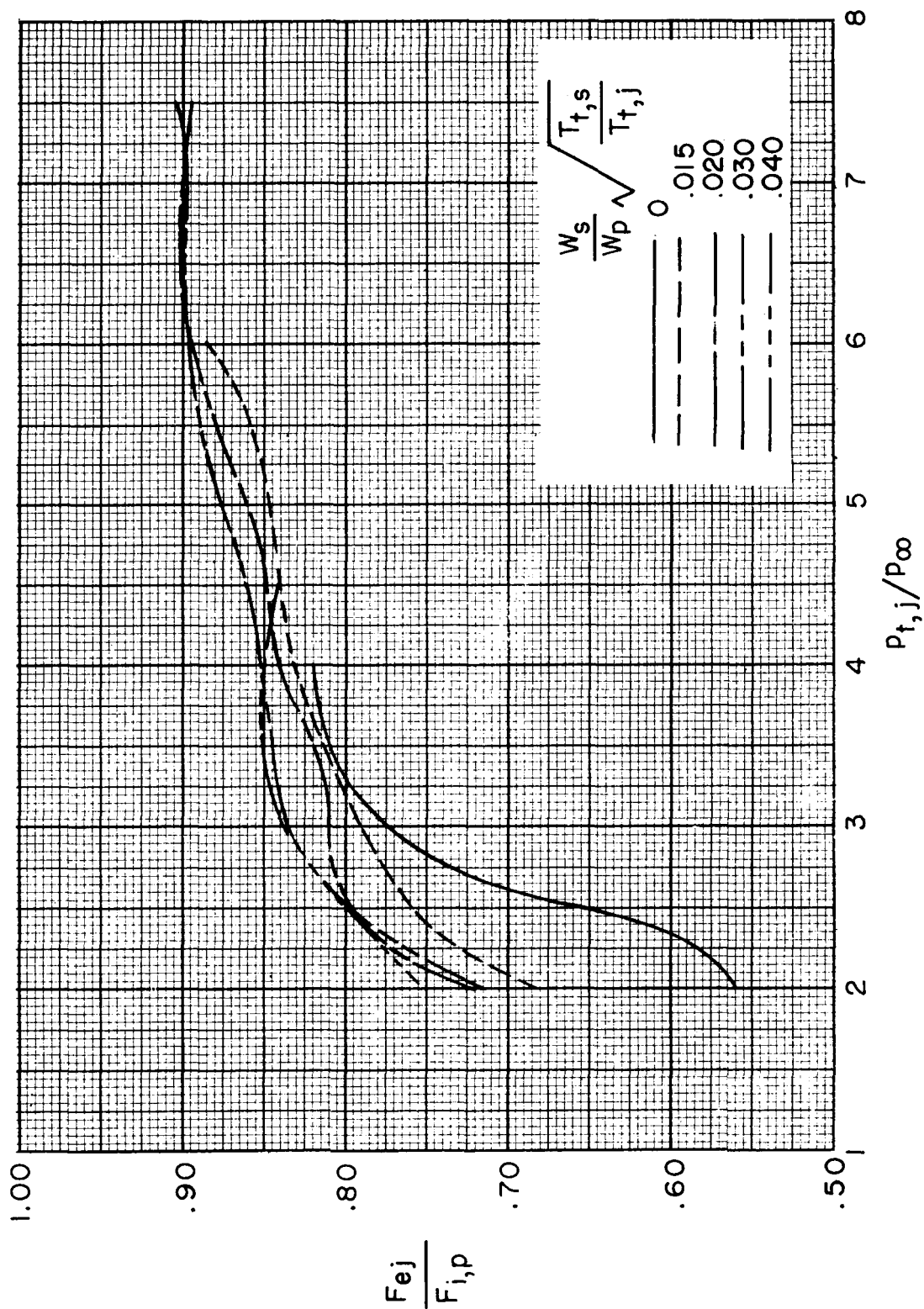


(f)  $M = 0.95$ ; afterburning nozzle.

Figure 14.- Continued.

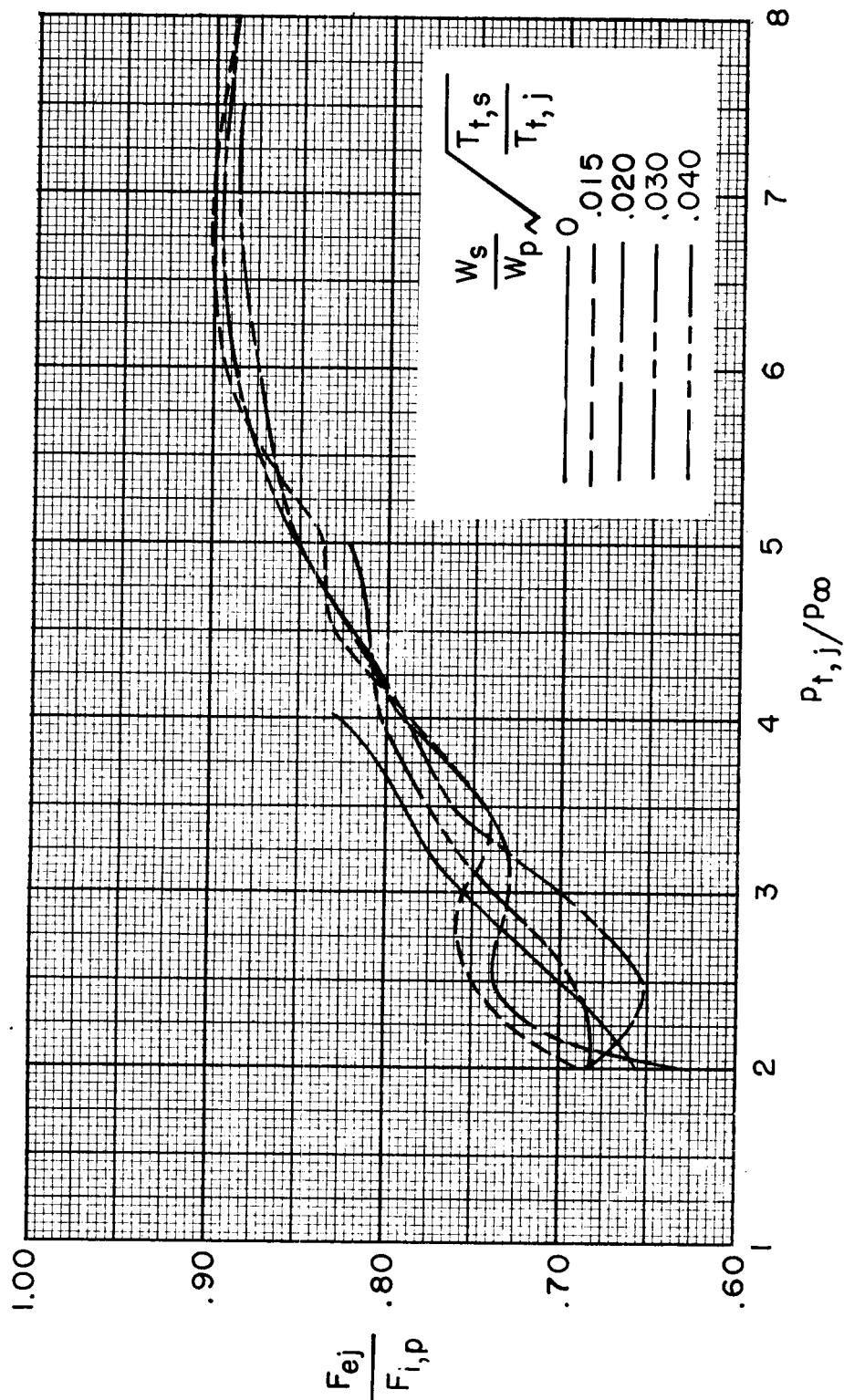
CONFIDENTIAL





(g)  $M = 1.00$ ; afterburning nozzle.

Figure 14.- Continued.



(h)  $M = 1.06$ ; afterburning nozzle.

Figure 14.- Concluded.

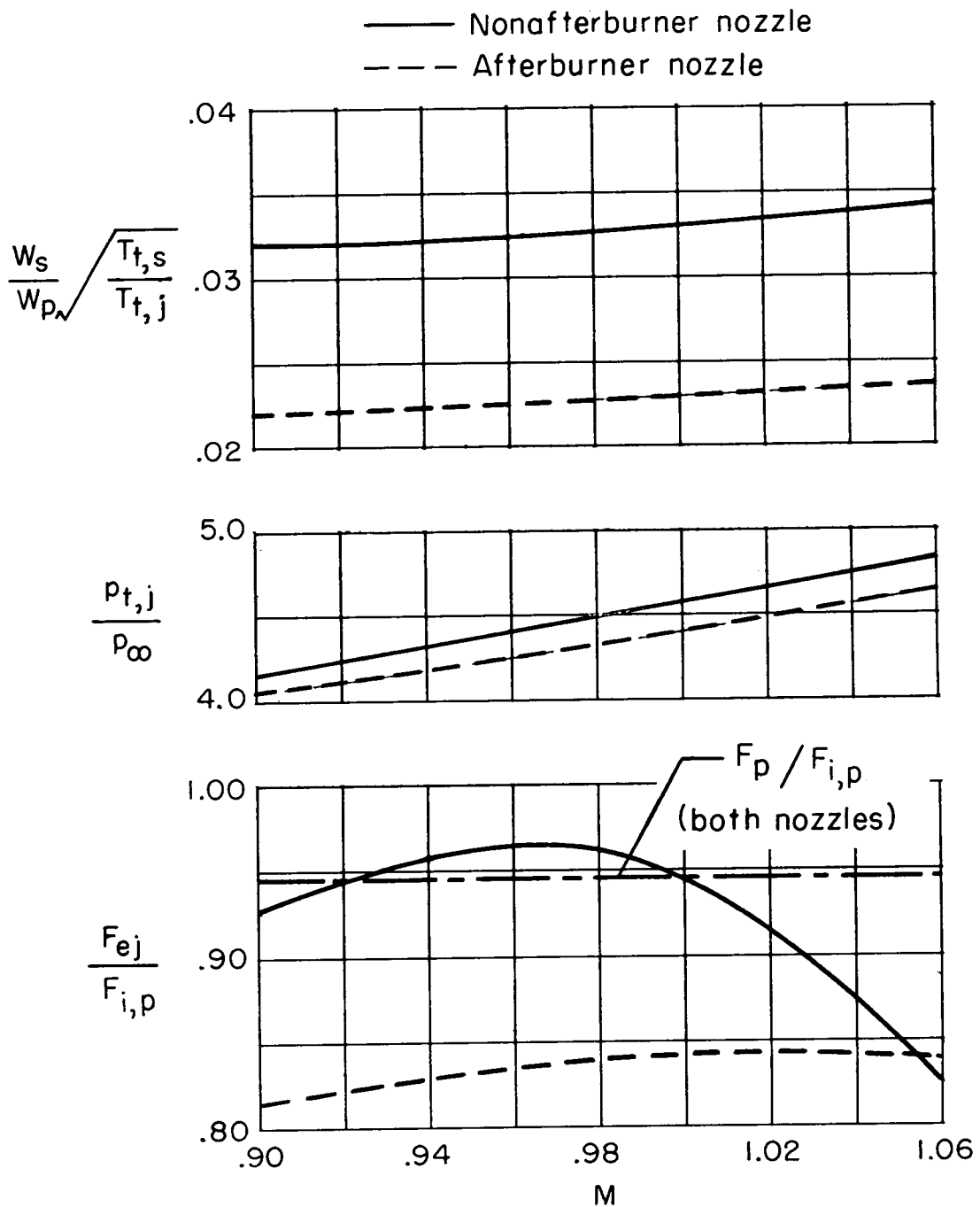


Figure 15.- Variation of ejector gross thrust ratio with Mach number at scheduled conditions.